Renewable Energy 220 (2024) 119628

Contents lists available at ScienceDirect

Renewable Energy

journal homepage: www.elsevier.com/locate/renene

Taguchi optimization and thermoelectrical analysis of a pin fin annular thermoelectric generator for automotive waste heat recovery

Wenlong Yang [a,b], Chenchen Jin [b], Wenchao Zhu [b,c,**], Yang Li [d], Rui Zhang [b], Liang Huang [b], Changjun Xie [a,b,*], Ying Shi [b]

[a] Hubei Key Laboratory of Advanced Technology for Automotive Components, Wuhan University of Technology, Wuhan, 430070, China
[b] School of Automation, Wuhan University of Technology, Wuhan, 430070, China
[c] State Key Laboratory of Advanced Technology for Materials Synthesis and Processing, Wuhan University of Technology, Wuhan, 430070, China
[d] Department of Electrical Engineering, Chalmers University of Technology, Gothenburg, 41258, Sweden

ARTICLE INFO

Keywords:
Annular thermoelectric generator
Pin fin
Taguchi method
Multiphysics numerical model
Heat exchanger

ABSTRACT

Enhancing thermoelectric performance while minimizing exhaust back pressure is a crucial step in advancing the commercial viability of automotive thermoelectric generators. To achieve high overall performance in a thermoelectric generator, an annular thermoelectric generator equipped with circular pin fins is proposed. A comprehensive three-dimensional numerical model is established to accurately predict thermoelectric performance and thermomechanical behavior. Detailed multi-physics field distribution characteristics are analyzed. Using an L_{25} orthogonal array, we examine five influencing factors and their five levels: exhaust temperature, exhaust mass flow rate, fin height, fin diameter, and the number of fins. The Taguchi analysis suggests that exhaust temperature is the most influential factor in determining thermoelectric performance, followed by mass flow rate, fin height, fin diameter, and fin number. The optimal values for these parameters are 673 K, 30 g/s, 20 mm, 3 mm, and 420, respectively. Under the optimal design parameters, the net power reaches 34.11 W, representing an 18.7% increase compared to the original design. Moreover, a comparative study is conducted between plate fins and pin fins, showing that the pin fin-based thermoelectric generator exhibits a 5.83% increase in output power and a 4.82% increase in maximum thermal stress compared to the plate fin-based thermoelectric generator.

1. Introduction

For modern engines, approximately 50% of the fuel energy is emitted into the atmosphere as exhaust gas [1]. Out of the remaining 50%, roughly 25% is employed to operate various equipment, with only 25% being dedicated to propelling the vehicle [2]. Improving the energy conversion efficiency of automobiles is consistently regarded as one of the key strategies for preserving precious fossil fuel resources and mitigating greenhouse gas emissions [3,4]. To enhance the fuel economy of automobiles [5,6], traditional techniques such as exhaust gas recirculation [7] and turbocharging [8] have been extensively researched.

Among various waste heat utilization technologies [9,10], thermoelectric power generation technology has garnered significant attention for its potential applications in automotive waste heat recovery systems. This interest arises from its distinct advantages, including the absence of moving parts, emissions, maintenance costs, quiet operation, and long service life. When a thermoelectric generator (TEG) is employed for waste heat recovery in a vehicle's diesel engine, its power generation potential can reach approximately 1000 W [11], which effectively fulfills the onboard equipment's power requirements. An automotive waste heat recovery TEG system typically consists of three main components: a thermoelectric power generation module, a heat exchanger for extracting heat energy, and a radiator. Consequently, the key aspects of TEG system optimization design generally revolve around these three elements.

Currently, automotive thermoelectric generators are still undergoing research and testing, and they have not yet found widespread use in commercial applications. The primary barriers to the broad adoption of TEGs in automotive waste heat recovery systems stem from limitations in the properties of thermoelectric materials and the challenge of

* Corresponding author. Wuhan university of technology, No.122, Luoshi road, Hongshan district, Wuhan city, Hubei province, China.
** Corresponding author. School of Automation, Wuhan University of Technology, Wuhan, 430070, China.
E-mail addresses: wenlongyang@whut.edu.cn (W. Yang), zhuwenchao@whut.edu.cn (W. Zhu), jackxie@whut.edu.cn (C. Xie).

https://doi.org/10.1016/j.renene.2023.119628
Received 26 June 2023; Received in revised form 9 October 2023; Accepted 11 November 2023
Available online 16 November 2023

Nomenclature

c	specific heat, J/(kg·K)
$C_{1\varepsilon}$,$C_{2\varepsilon}$, $C_{3\varepsilon}$, C_{μ}	constants
D	The diameter of pin fin, mm
$\overline{\overline{E}}$	Young's modulus, Gpa
$\vec{E}$	electric field intensity vector, V/m
f	characteristic property
H	height of pin fin, mm
h	heat transfer coefficient, W/(m^2•K)
I	current, A
$\vec{J}$	electric current density vector, A/m^2
k	turbulence kinetic energy
m	mass flow rate, g/s
n	number of pin fins
P_{loss}	power loss, W
P_{net}	net power, W
P_{out}	output power, W
ΔP	pressure drop, Pa
Q	heat flow, W
R	resistance, Ω
R_L	load resistance, Ω
S	Seebeck coefficient, V/K
S/N	signal-to-noise ratio
T	temperature, K
U	voltage, V

Greek symbols

α	Coefficient of thermal expansion, 10^{-6}/K
$\alpha\Delta T$	Seebeck electromotive force, V
ε	friction loss coefficient
η	efficiency, %
λ	Thermal conductivity, W/(m•K)
μ	Poisson's ratio
ρ	Density, Kg/m
σ^{-1}	Electrical conductivity, Ω•m
φ	electric potential, V

Subscript

a	hot air
at	ambient temperature
c	cold end
ce	Ceramic substrate
co	electrode slices
eff	effective
n	N-type thermoelectric leg
p	P-type thermoelectric leg

Abbreviations

ATEM	annular thermoelectric module
ATEG	annular thermoelectric generator
TEM	thermoelectric module
TEG	thermoelectric generator

achieving high heat recovery efficiency from vehicle exhaust. This challenge arises because methods aimed at improving heat collection efficiency by increasing fluid turbulence in the automotive exhaust system can have adverse effects on the engine, leading to a significant rise in exhaust back pressure. This results in the engine producing parasitic power, ultimately reducing overall fuel efficiency. Therefore, one of the primary technical challenges currently lies in enhancing heat transfer and boosting thermoelectric conversion efficiency while ensuring that the exhaust pressure drop remains within an acceptable range.

There are two primary approaches to enhance the efficiency of thermoelectric power generation modules: material optimization and geometric optimization. Progress in thermoelectric materials demands the development of new materials with a high figure of merit [12]. Crucially, optimizing the minimum building unit (PN leg) of thermoelectric modules can improve the power generation module's efficiency while reducing the required amount of thermoelectric material. The effects of significant parameters, such as leg length [13], cross-sectional area [14], leg number, and filling ratio [15], on the thermoelectric performance in the geometric optimization of thermoelectric legs have been extensively explored. However, these studies have primarily focused on flat thermoelectric generators with rectangular PN legs. In practical applications, cylindrical heat sources are common, making annular PN legs more suitable for integration with annular heat exchangers. This configuration helps reduce thermal resistance caused by geometric mismatch [16]. An annular thermocouple has been proposed as a replacement for the traditional flat thermocouple [17]. The annular thermoelectric generator (ATEG) adopts a ring-shaped design, with annular thermoelectric materials installed within the curved substrate layer, allowing for higher thermoelectric conversion efficiency within cylindrical heat sources. Furthermore, due to its relatively compact size, it can be conveniently integrated into various equipment for broader applications. Researchers addressed and compared the multi-objective optimization problems of a PN couple, an annular thermoelectric module, and an ATEG [18]. They have suggested that structural optimization should be based on the complete ATEG rather than just a single PN leg.

Optimization research for the heat exchanger and radiator in automotive TEGs aims to enhance their heat transfer capabilities with the thermoelectric modules (TEMs). Improved heat transfer capabilities result in a greater temperature difference, leading to enhanced TEG performance. To illustrate, a hexagonal TEG with three TEMs on each surface was constructed, using a hybrid powertrain internal combustion engine as the heat source [19]. Experimental results demonstrated that the utilization of 18 TEMs yielded a maximum output power of 8.2 W and a maximum efficiency of 6.18%. In another approach, a dual-pore cylinder object was introduced to intensify fluid disturbance in the hot gas channel, resulting in a 12.9% power increase compared to the channel without the porous object [20]. Additionally, the incorporation of circulating heat transfer fluid into TEG hot-side heat exchangers for automobiles has been explored [21]. This method leverages the high heat transfer coefficient of the circulating thermal fluid to enhance the thermoelectric system's performance [22]. Simulation results indicated that, compared to traditional generator sets, the peak net output power of the new generator set could be increased by 77.5%, while reducing the number of components by 83.2%. In contrast to commonly used heat exchangers [23,24], the adoption of phase change materials has emerged as a reliable method for maintaining temperature stability at the hot and cold ends. This approach improves TEG heat transfer, enhances temperature uniformity, and increases TEM heat extraction capacity [25]. However, this method is difficult and costly to install in automotive TEGs.

To enhance the heat transfer efficiency in the hot channel, the installation of fins stands out as a low-cost, structurally simple, and highly efficient method [26]. A study was conducted to experimentally assess the thermal performance of radiators with and without fins [27]. The results indicated that the RT-44 type triangular pin fins arranged internally and staggered exhibited superior heat dissipation effects. In another study, numerical simulations were employed to investigate the potential of a perforated array of small wing vortex generators in improving the heat transfer efficiency of finned tube heat exchangers

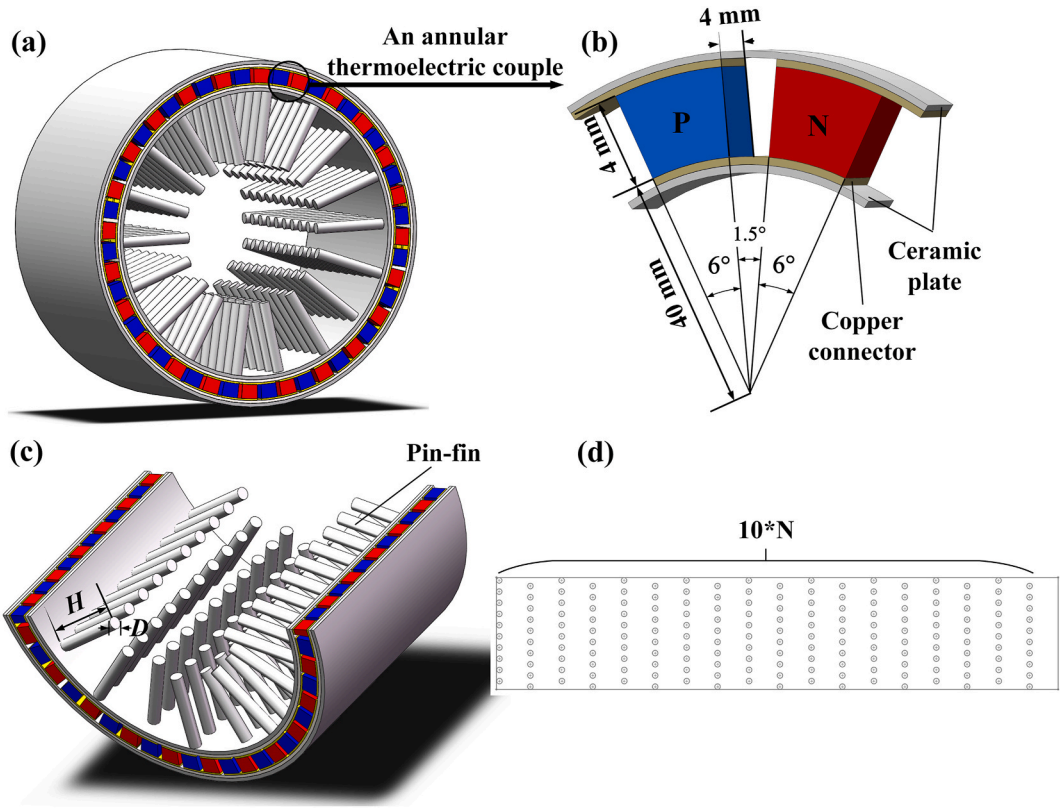

Fig. 1. System schematic: (a) Overall structure, (c) An annular thermocouple, (b) Heat exchanger cross-section, (d) fin distribution (expanded view).

[28]. These simulations demonstrated that the array with discontinuous small wings achieved the most significant enhancement in heat transfer. In comparison to ordinary fins, the heat transfer coefficient increased by 8.70−6.43% at 33°, with a pressure drop loss of 4.97−2.30%. The electricity generation performance of automotive TEGs under transient conditions was examined by incorporating plate fins into a rectangular tube [29]. The numerical results revealed that changes in exhaust temperature exhibited a certain delay in the output response, often accompanied by variations in output voltage and power with changes in exhaust mass flow rate. By installing denser fins downstream of the heat exchanger, significant improvements in output power and net power were achieved, with an average increase of 189.1% and 177.4%, respectively [30]. Fins, a commonly employed method to enhance heat transfer, have been extensively studied in flat thermoelectric generators. Designing heat exchangers based on innovative fin structures proves to be an effective approach for enhancing heat transfer performance [31].

The study of cylindrical heat exchangers has been relatively limited, primarily due to the high cost associated with designing thermoelectric modules in a ring shape to fit the curved hot end surface of the exchanger [32]. Researchers conducted a comparative analysis of the performance between ring-shaped and flat thermoelectric generators for cylindrical heat sources, demonstrating that the ring-shaped TEG proves to be a superior choice, especially when the inlet temperature or convective heat transfer coefficient is relatively high [33]. Consequently, there is a growing research interest in improving heat transfer and adapting the structure for cylindrical heat exchangers and ring-shaped TEMs [34]. A concentric ring-shaped thermoelectric generator was introduced, comprising a ring-shaped TEM and a concentric ring-shaped heat exchanger [35]. This design improved the heat transfer coefficient and increased the maximum net power by 65% compared to traditional ATEGs. However, it's worth noting that this structure involves higher modification costs when compared to the installation of fins. In another approach, a metal spoiler was incorporated into the annular exhaust channel of an air-to-air thermoelectric generator, and the geometric parameters of the optimal spoiler were fine-tuned using a meta-heuristic algorithm [36]. This modification led to a 10.41% increase in net power and a 22.51% improvement in efficiency compared to an ATEG without a spoiler.

Plate fins and pin fins represent two types of enhanced heat transfer methods with strong heat transfer performance and lower material costs, rendering them suitable for automotive thermoelectric generator systems. When designing heat exchangers, it's crucial to consider not only heat transfer performance but also the fluid's resistance characteristics [37]. While fins have been widely used to enhance thermoelectric performance, most previous research has concentrated on integrating plate fins into rectangular pipes to improve the thermal energy collection efficiency of traditional flat TEGs. Notably, there has been a dearth of design research focused on incorporating fins into cylindrical heat exchangers tailored for annular thermoelectric generators. The applicability of research results and design guidelines derived from flat TEGs has not been validated in the context of cylindrical pipes and annular TEGs. Circular pin fins, in particular, have demonstrated exceptional heat transfer efficiency and can achieve a higher heat transfer coefficient compared to plate fins [38,39]. This structure is especially well-suited for enhancing heat transfer in cylindrical pipes as it maintains relatively low pressure drop while improving heat transfer efficiency [40]. Based on an extensive literature review, there is a scarcity of existing research on the numerical prediction and optimization of the thermal-electric performance and thermomechanical performance of circular pin fins in annular thermoelectric generators under fluid-solid heat coupling conditions. Therefore, this study aims to address these research gaps.

To enhance the thermoelectric conversion efficiency of annular thermoelectric generators in automobiles, while ensuring that the exhaust pressure drop and thermal stresses on the thermoelectric modules remain within acceptable limits, this study proposes an improved heat transfer design involving the integration of pin fins within the circular thermoelectric generator. Taking into consideration fluid-solid

Table 1
Material properties of the ATEG system.

Component	Material	ρ (Kg·m^{-3})	λ (W/(m·K))	S (V/K)	σ^{-1} (Ω·m)	(Gpa)	μ	α (10^{-6}K^{-1})
Heat exchanger and radiator	Aluminum	3970	217.7	N/A	N/A	380-366 (273–600 K)	0.26	4.89–6.68 (273–600 K)
P-type material	Bi_2Te_3	6858	$\lambda_p(T)$	$S_p(T)$	$\sigma_p^{-1}(T)$	radial:40.3 axial:49.7	0.28	16.8
N-type material	Bi_2Te_3	7858	$\lambda_n(T)$	$S_n(T)$	$\sigma_n^{-1}(T)$	radial:42.7 axial:51	0.28	16.8
Electrode slices	Copper	8940	165.64	N/A	1.75×10^{-8}	119-100 (273–600 K)	0.31	1.67–1.76 (273–600 K)
Ceramic substrate	porcelain	255	18	N/A	N/A	N/A	N/A	N/A

Table 2
Thermoelectric properties of the Bi_2Te_3-based material [16].

Name	Seebeck coefficient S (V/K)	Thermal conductivity λ (W/m·K)	Electrical resistivity σ^{-1} (Ω·m)
P-type material	$S_p(T) = 1.134 \times 10^{-14}T^4 - 2.035 \times 10^{-11}T^3 + 1.11 \times 10^{-8}T^2 - 1.818 \times 10^{-6}T + 1.61 \times 10^{-4}$	$\lambda_p(T) = -1.242 \times 10^{-9}T^4 + 2.331 \times 10^{-6}T^3 - 1.575 \times 10^{-3}T^2 + 0.457T - 46.97$	$\sigma_p^{-1}(T) = -4.32 \times 10^{-16}T^4 + 8.94 \times 10^{-13}T^3 - 7.74 \times 10^{-10}T^2 + 3.519 \times 10^{-7}T - 5.01 \times 10^{-5}$
N-type material	$S_n(T) = -1.3 \times 10^{-14}T^4 + 2.325 \times 10^{-11}T^3 + 1.42 \times 10^{-8}T^2 + 3.469 \times 10^{-6}T - 4.428 \times 10^{-4}$	$\lambda_n(T) = 1.537 \times 10^{-10}T^4 - 3.019 \times 10^{-7}T^3 + 2.246 \times 10^{-4}T^2 - 7.414 \times 10^{-2}T + 10.12$	$\sigma_n^{-1}(T) = 1.317 \times 10^{-16}T^4 - 2.305 \times 10^{-13}T^3 + 7.827 \times 10^{-11}T^2 + 4.507 \times 10^{-8}T - 8.072 \times 10^{-6}$

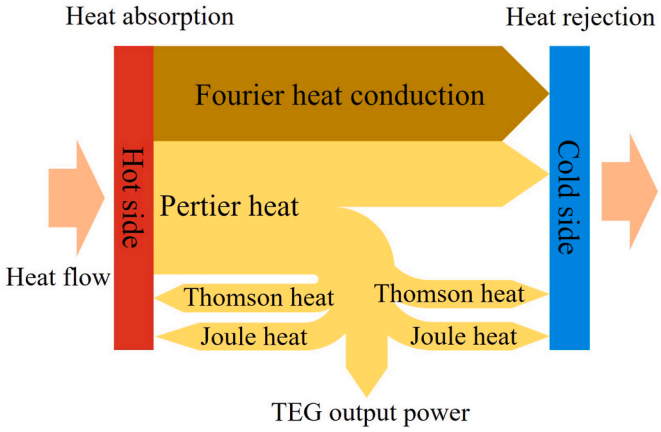

Fig. 2. Energy flow of thermoelectric generator.

coupling and all thermoelectric effects, the optimal combination of operating conditions, pin fin structures, and quantities are optimized. Additionally, the impact of pin fins on the thermal-mechanical performance of the ATEM is investigated. This study encompasses the following key aspects: Firstly, a comprehensive multi-physics numerical model of fluid-thermal-solid-electric coupling is established using a 3-D finite element method to investigate the influence of circular pin fins on ATEG performance. Secondly, an L_{25} orthogonal matrix is constructed, and the Taguchi method is utilized to investigate the sensitivity of operating conditions and pin fin parameters on the net power and conversion efficiency. This systematic approach allows for the determination of the optimal parameter combination that maximizes performance. Finally, the effects of different fin structures on the thermomechanical performance of the ATEG are analyzed. The findings of this research provide valuable guidance for the optimization and modeling of automotive ATEGs.

2. Model development

2.1. Physical model

The ATEG consists of three key components: a heat exchanger, annular thermoelectric modules, and a radiator. Fig. 1(a) provides a schematic illustration of a pin-finned ATEG. The heat exchanger features a cylindrical channel with a diameter of 80 mm and a length of 60 mm. To enhance heat transfer, aluminum pin fins with specific height (H) and diameter (D) dimensions are strategically placed within the channel. Each pin fin extends axially along the vehicle exhaust pipe, as shown in Fig. 1(c). To simplify the representation of the fin layout, the circular channel is represented as a flat schematic diagram in Fig. 1(d). Along the fluid flow direction, ten pin fins are installed initially, with a total of 10 × N pin fins being added as needed. To further improve the heat transfer coefficient, different rows of circular pin fins are arranged in a cross configuration.

The outer surface of the circular channel is encased with a layer of annular thermoelectric modules, which represent a pivotal component of the system. The ATEM comprises 12 rings, with each ring housing 24 pairs of annular thermocouples, as illustrated in Fig. 1(b). Each thermocouple consists of a pair of PN legs, conductive copper electrode slices, and ceramic plates. These annular thermocouples are interconnected in a thermal parallel and electrical series arrangement, collectively forming a power generation module. Each individual thermocouple boasts a height and thickness of 4 mm, featuring an individual leg angle of 6° and an angle of 1.5° between each leg. The gap between the rings measures 1 mm. To complete the TEM circuit, a load resistor with dimensions of 5 × 5 × 20 mm^3 is connected at both ends. The magnitude of the load resistance can be adjusted by modifying the resistivity value. The outermost layer comprises a radiator, which typically employs a concentric sleeve as a conduit for cooling water [35]. For simplicity, the cooling system is not depicted in the diagram. Throughout the simulation process, it was assumed that the hot and cold fluids enter the heat exchanger through their respective inlets at specific temperatures and mass flow rates. This simulation aimed to replicate the forced convection conditions experienced in automotive TEG systems, involving hot exhaust gases from the engine and cooled water circulated by the pump. To enhance the heat transfer efficiency, the cold and hot fluids flow in opposite directions [41]. Table 1 presents the detailed parameters of the ATEG. The thermoelectric properties of the PN semiconductor exhibit significant temperature dependence, as shown in Table 2.

2.2. Governing equations

As the engine exhaust enters the annular pin fin heat exchanger and heats the hot end, the cold end is simultaneously kept cool by the coolant, creating a significant temperature difference across the ATEMs. This temperature differential triggers the diffusion and drift motion of charge carriers within the thermoelectric semiconductor. Consequently, positive and negative charges accumulate at the hot and cold ends of the semiconductor, respectively, giving rise to an electrostatic field. Once the motion of charge carriers reaches equilibrium, the thermoelectric

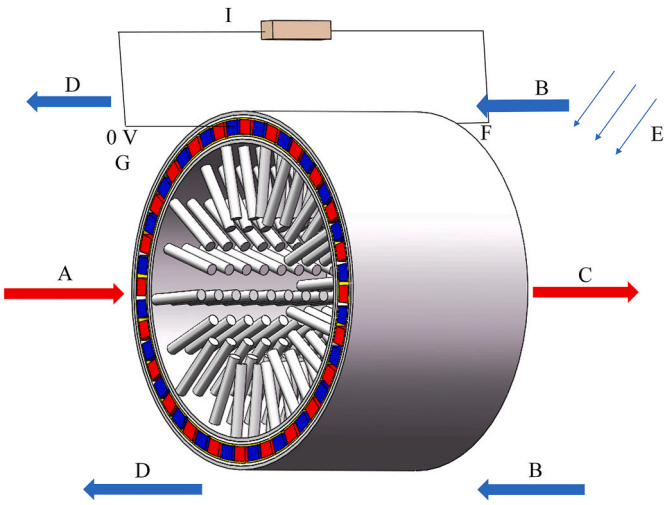

Fig. 3. Boundary conditions of the ATEG. A: exhaust mass flow inlet, B: water inlet, C: exhaust pressure outlet, D: water outlet, E: ambient convection heat transfer, F: voltage coupling boundary, and G: Grounded boundary.

Table 3
Selected 5 factors and the levels.

Factor	Parameter	Level 1	Level 2	Level 3	Level 4	Level 5
A	Temperature, T_a (K)	473	523	573	623	673
B	Mass flow rate, m_a (g/s)	20	25	30	35	40
C	Height, H (mm)	10	15	20	25	30
D	Diameter, D (mm)	1	1.5	2	2.5	3
E	Number, n	10 × 18	10 × 24	10 × 30	10 × 36	10 × 42

semiconductor efficiently converts heat energy into electrical energy, resulting in the generation of current within the circuit.

The energy flow within the ATEG is depicted in Fig. 2. This current flow, in turn, influences the heat distribution within the heat exchanger due to the Peltier effect and Joule heating. Consequently, the model necessitates the consideration of multi-physics fields, including thermal, fluid, and electric fields, necessitating simultaneous solutions of the control equations for these three fields. In this section, we provide a comprehensive description of the heat transfer equations and boundary conditions employed in the steady-state three-dimensional numerical model. The following assumptions are made:

(1) The thermoelectric material is isotropic; (2) Gravity is ignored; (3) Radiation heat is ignored; (4) The heat flow is in a steady-state condition.

As the Mach numbers of the exhaust gas and cooling water are quite low, they can be considered incompressible. Additionally, the *k*-epsilon (*k*-*ε*) turbulence model, based on renormalization group theory, is employed for its higher adaptability and precision compared to other models. The detailed governing equations for the fluid field are as follows [42,43]:

$$\nabla \cdot (v) = 0 \tag{1}$$

$$\nabla \cdot (vv) = -\frac{1}{\rho}\nabla p + \nabla \cdot (\mu \nabla v) \tag{2}$$

$$\nabla \cdot (\lambda \nabla T) = \rho c v \cdot \nabla T \tag{3}$$

$$\frac{\partial}{\partial t}(\rho k) + \frac{\partial}{\partial x_i}(\rho k u_i) = \frac{\partial}{\partial x_j}\left[\alpha_k \mu_{eff}\frac{\partial k}{\partial x_j}\right] + G_b + G_k - Y_M - \rho\varepsilon \tag{4}$$

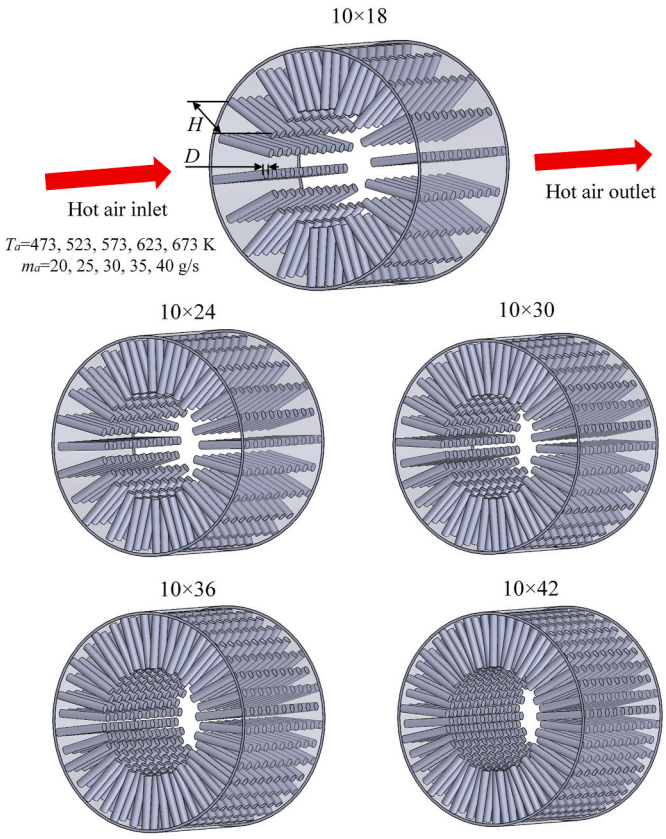

Fig. 4. Circular pin fins in various configurations.

$$\frac{\partial}{\partial t}(\rho\varepsilon) + \frac{\partial}{\partial x_i}(\rho\varepsilon u_i) = \frac{\partial}{\partial x_j}\left[\alpha_\varepsilon \mu_{eff}\frac{\partial \varepsilon}{\partial x_j}\right] + C_{1\varepsilon}\frac{\varepsilon}{k}(C_{3\varepsilon}G_b + G_k) - C_{2\varepsilon}\rho\frac{\varepsilon^2}{k} - R_\varepsilon \tag{5}$$

Where k is the turbulent kinetic energy, G_b is the turbulent kinetic energy generated by buoyancy, and G_k is the turbulent kinetic energy generated by the mean velocity gradient. Y_M represents the contribution of pulsating expansion, while ∂_k and ∂_ε represent the inverse effective Prandtl numbers of k and ε. Eqs. (1)–(3) are the conservation of mass, momentum, and energy of the fluid in the flow channels of heat exchangers and radiators, while Eqs. (4 and (5) represent the transport equations of the RNG *k*-*ε* model.

When calculating the temperature distribution of solid components (including thermocouples, copper sheets, ceramic plates, heat exchangers, and radiators), the main governing equation is energy conservation, i.e.,

$$\nabla \cdot (\lambda \nabla T) = 0 \tag{6}$$

In this model, various thermoelectric effects, including Fourier heat conduction, Joule heating, the Peltier effect, and the Thomson effect, are considered. Consequently, the heat variations resulting from these effects need to be accounted for in the energy conservation differential equation. Eqs. 7–10 [44] depict the energy conservation equations for the p-type thermoelectric semiconductor leg, n-type thermoelectric semiconductor leg, electrode slices, and ceramic plate.

$$\nabla \cdot \left(\lambda_p(T)\nabla T_P\right) = -\rho_P(T)\vec{J}^2 + \nabla S_P(T)\vec{J}T_P \tag{7}$$

$$\nabla \cdot (\lambda_n(T)\nabla T_n) = -\rho_n(T)\vec{J}^2 + \nabla S_n(T)\vec{J}T_n \tag{8}$$

$$\nabla \cdot (\lambda_{co}\nabla T) = -\rho_{co}\vec{J}^2 \tag{9}$$

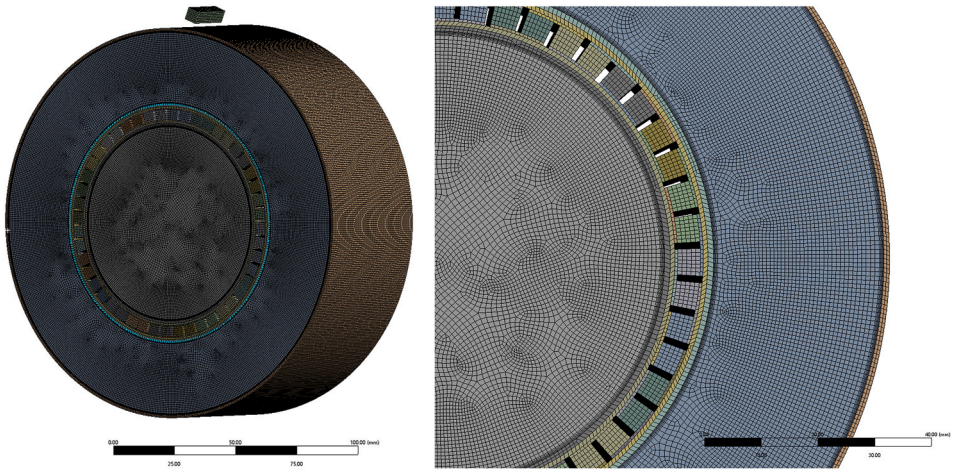

Fig. 5. Finite element model of the ATEG.

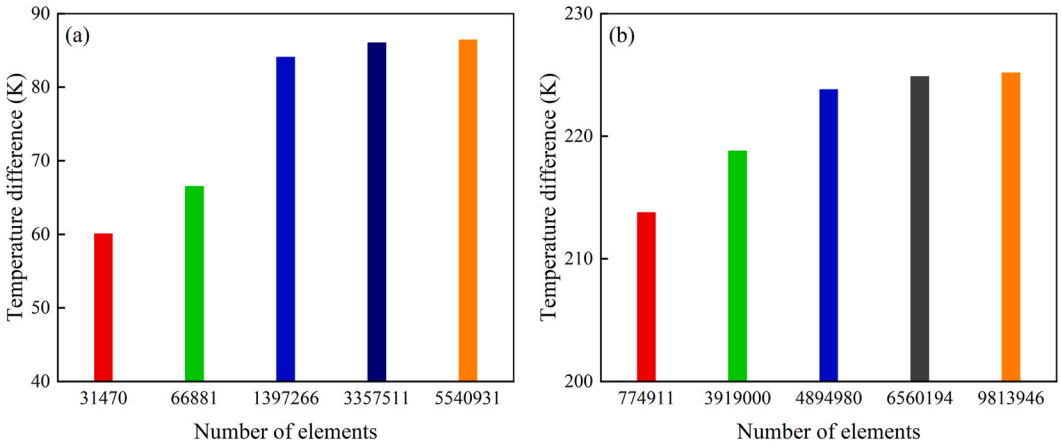

Fig. 6. Grid independence test (a) without pin fins installed and (b) with pin fins installed.

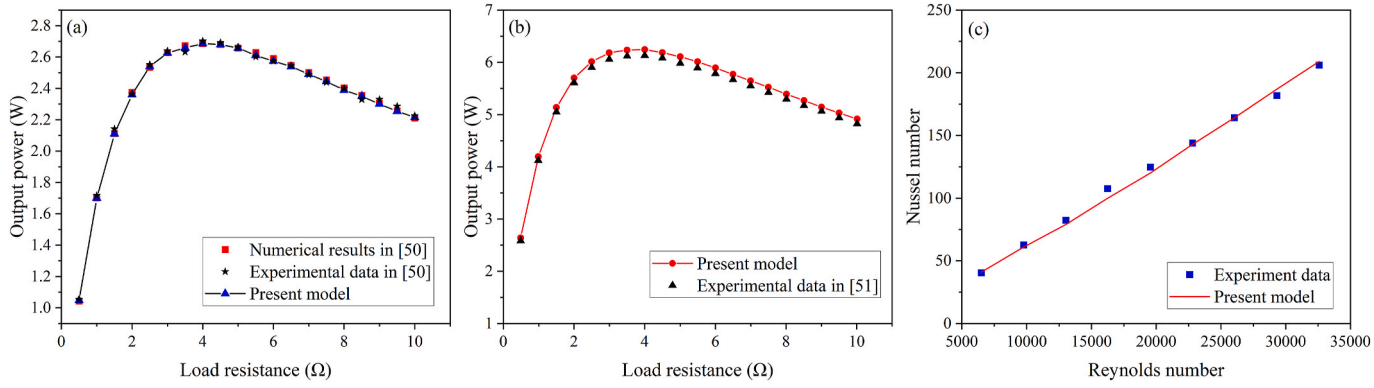

Fig. 7. Validation of (a) thermoelectric generation model, (b) conduction-convection model, and (c) Turbulence model.

$$\nabla \cdot (\lambda_{ce} \nabla T) = 0 \tag{10}$$

The electric field intensity vector is defined as:

$$\vec{E} = -\nabla\varphi + \alpha \nabla T \tag{11}$$

Where φ represents the potential and $\alpha\Delta T$ represents the Seebeck electromotive force.

Current density vector $\vec{J}$ can be expressed as:

$$\vec{J} = \sigma E \tag{12}$$

Where σ represents the electrical conductivity.

The governing equation of charge can be expressed as:

$$\nabla \cdot \vec{J} = 0 \tag{13}$$

The power loss due to exhaust backpressure is expressed as follows:

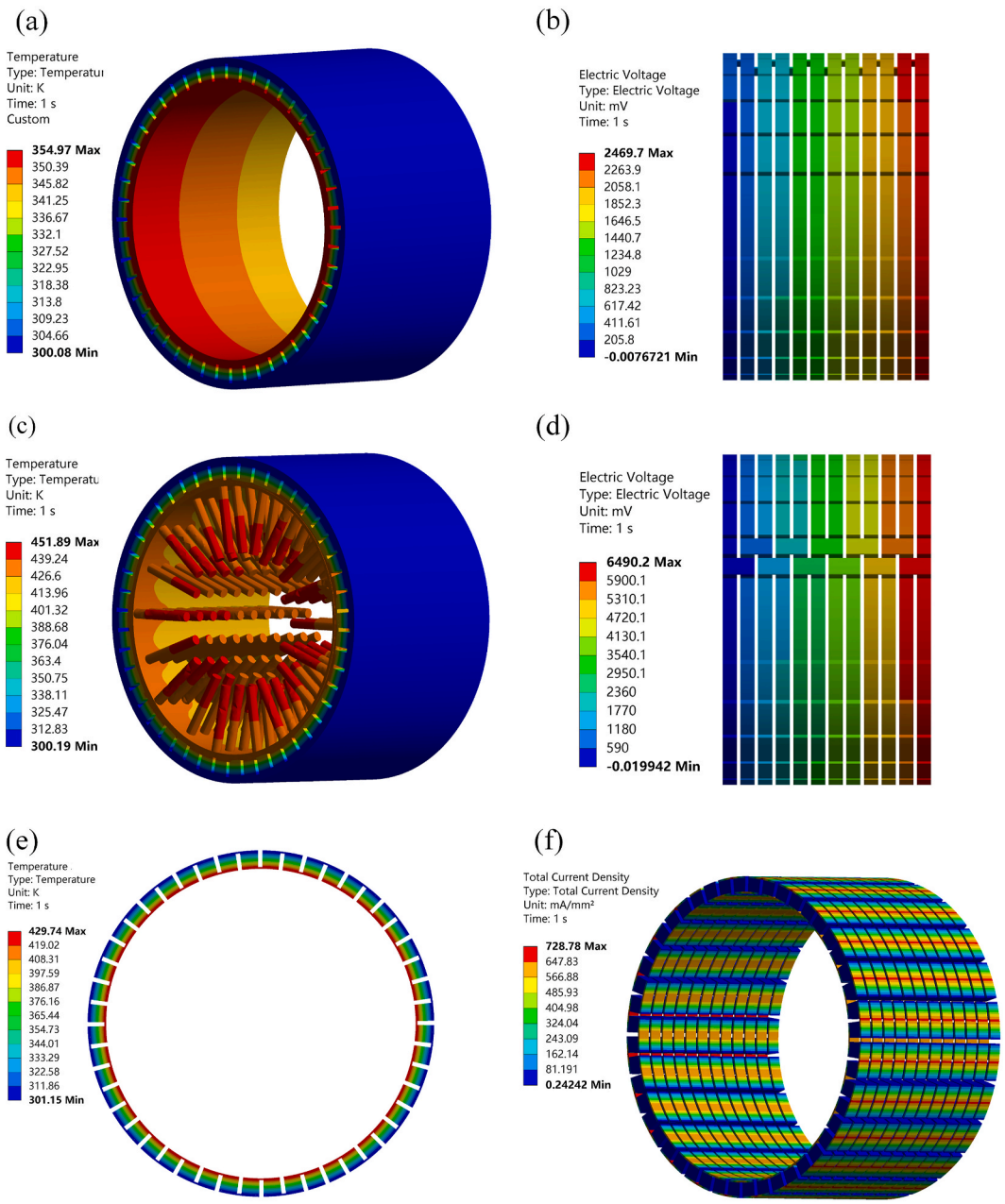

Fig. 8. Numerical results of ATEG at $T_a = 523$ K and $m_a = 25$ g/s. (a) Surface temperature distribution and (b) electric potential distribution of the smooth pipe heat exchanger ATEG. (c) Surface temperature distribution, (d) electric potential distribution, (e) PN leg's temperature distribution, and (f) current density distribution of the pin fin heat exchanger ATEG.

$$P_{loss} = (P_1 - P_2)\cdot m_a / \rho \tag{14}$$

Here, P_1 and P_2 denote the average pressure on the inlet and outlet surfaces, respectively. m_a and ρ denote the mass flow rate and density of the hot fluid.

The output power of the ATEG is calculated using the following equation:

$$P_{out} = \frac{U^2}{R_L} \tag{15}$$

Where U represents the output voltage and R_L represents the load resistance.

The net power and efficiency are expressed as follows:

$$P_{net} = P_{out} - P_{loss} \tag{16}$$

$$\eta = \frac{P_{out}}{Q_h} \tag{17}$$

Thermal stresses arise in a thermoelectric module as a result of the disparity between the thermal expansion coefficients of the materials within the module and the external constraints. Specifically, in this pin fin thermoelectric generator system, the inclusion of pin fins modifies the temperature distribution along the PN legs. To assess the thermodynamic performance of the ATEG under different heat exchanger structures, the displacement-strain relationship is determined based on the following dimensionless equations [45]:

$$\overline{\varepsilon}_{xx} = \frac{\partial \overline{u}}{\partial \overline{x}}, \overline{\varepsilon}_{yy} = \frac{\partial \overline{v}}{\partial \overline{y}}, \overline{\varepsilon}_{zz} = \frac{\partial \overline{w}}{\partial \overline{z}} \tag{18}$$

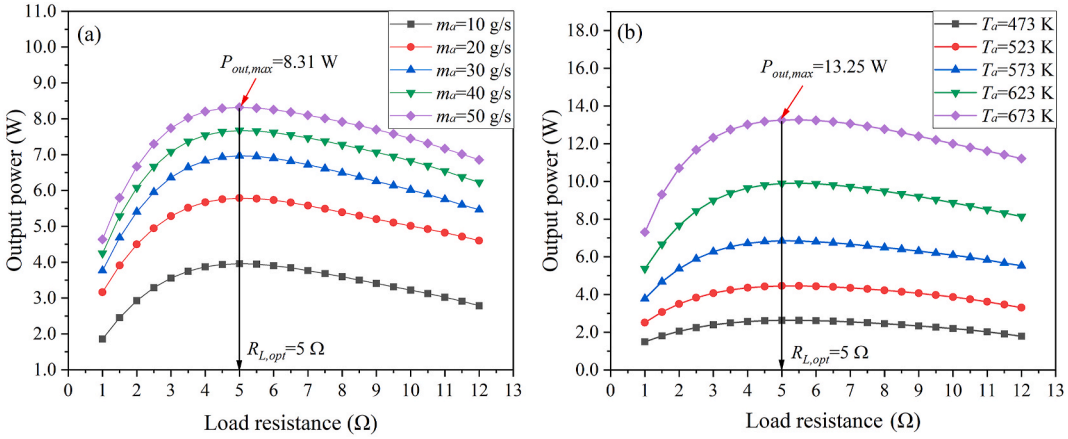

Fig. 9. The impact of load resistance on the output power of the pin fin ATEG under different exhaust (a) mass flow rates and (b) temperatures.

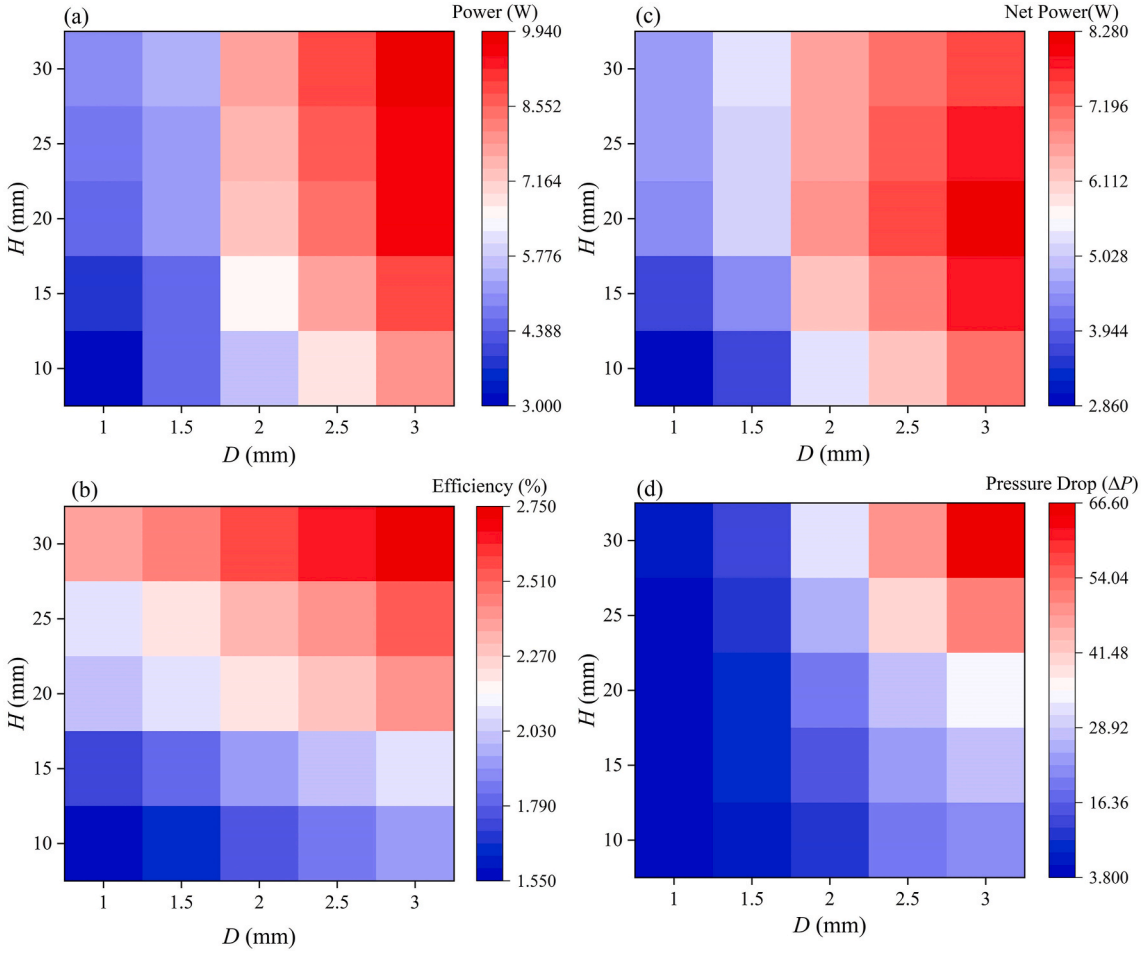

Fig. 10. Effects of the pin fin's structural parameters on (a) power output, (b) efficiency, (c) net power, and (d) pressure drop.

Table 4
Level combination of the size of the pin–fin and boundary conditions in L_{25} (5^6) orthogonal array.

Run	Factor A	Factor B	Factor C	Factor D	Factor E	P_{net} (W)	$(S/N)_{Pnet}$	η (%)	$(S/N)_{\eta}$
1	1	1	1	1	1	1.094	0.784	0.681	−3.333
2	1	2	2	2	2	2.526	8.049	1.093	0.771
3	1	3	3	3	3	4.444	12.956	1.581	3.981
4	1	4	4	4	4	3.905	11.833	1.992	5.987
5	1	5	5	5	5	−3.177	10.037	2.242	7.013
6	2	1	2	4	5	9.384	19.448	2.141	6.612
7	2	2	3	5	1	7.796	17.838	1.984	5.952
8	2	3	4	1	2	4.387	12.843	1.461	3.292
9	2	4	5	2	3	7.305	17.273	2.064	6.292
10	2	5	1	3	4	6.273	15.949	1.889	5.524
11	3	1	3	5	4	10.970	20.804	2.286	7.181
12	3	2	4	1	5	17.061	24.640	2.925	9.323
13	3	3	5	2	1	13.043	22.307	2.592	8.272
14	3	4	1	3	2	10.543	20.460	2.374	7.508
15	3	5	2	4	3	7.071	16.990	1.874	5.456
16	4	1	4	2	3	24.288	27.708	3.359	10.52
17	4	2	5	3	4	13.953	22.893	2.597	8.290
18	4	3	1	4	5	12.660	22.048	2.485	7.905
19	4	4	2	5	1	11.687	21.354	2.408	7.633
20	4	5	3	1	2	19.105	25.623	3.167	10.012
21	5	1	5	3	2	22.999	27.234	3.237	10.204
22	5	2	1	4	3	18.188	25.196	2.946	9.385
23	5	3	2	5	4	28.736	29.169	3.590	11.103
24	5	4	3	1	5	19.649	25.867	3.078	9.764
25	5	5	4	2	1	16.169	24.174	2.831	9.039

$$\overline{\varepsilon}_{xy}=0.5\left(\frac{\partial\overline{u}}{\partial\overline{y}}+\frac{\partial\overline{v}}{\partial\overline{x}}\right),\overline{\varepsilon}_{yz}=0.5\left(\frac{\partial\overline{w}}{\partial\overline{y}}+\frac{\partial\overline{v}}{\partial\overline{z}}\right),\overline{\varepsilon}_{zx}=0.5\left(\frac{\partial\overline{w}}{\partial\overline{x}}+\frac{\partial\overline{u}}{\partial\overline{z}}\right) \tag{19}$$

The following asymmetric Jacobi matrix represents a dimensionless form of stress-strain relationship:

$$\begin{Bmatrix}\overline{\sigma}_{xx}\\ \overline{\sigma}_{yy}\\ \overline{\sigma}_{zz}\\ \overline{\sigma}_{yz}\\ \overline{\sigma}_{xz}\\ \overline{\sigma}_{xy}\end{Bmatrix}=\frac{\overline{E}}{(1+v)(1-2v)}\begin{bmatrix}1-v & v & v & 0 & 0 & 0\\ v & 1-v & v & 0 & 0 & 0\\ v & v & 1-v & 0 & 0 & 0\\ 0 & 0 & 0 & 1-2v & 0 & 0\\ 0 & 0 & 0 & 0 & 1-2v & 0\\ 0 & 0 & 0 & 0 & 0 & 1-2v\end{bmatrix}$$
$$\times\begin{Bmatrix}\overline{\varepsilon}_{xx}\\ \overline{\varepsilon}_{yy}\\ \overline{\varepsilon}_{zz}\\ \overline{\varepsilon}_{yz}\\ \overline{\varepsilon}_{xz}\\ \overline{\varepsilon}_{xy}\end{Bmatrix}-\begin{Bmatrix}1\\1\\1\\0\\0\\0\end{Bmatrix}\frac{\overline{\alpha}\overline{E}\overline{T}}{1-2\mathrm{v}} \tag{20}$$

The stress component is represented by σ_{ij} and the strain tensor is represented by ε_{ij}. Poisson's ratio is denoted by v, while $\overline{\alpha}$ and $\overline{E}$ respectively represent the linear thermal expansion coefficient and the Young's modulus of elasticity.

According to the above equation, this study utilizes the Fluent and Thermal-electric software of ANSYS2022 R1 for coupled simulation and solving the established numerical model.

2.3. Boundary conditions

The main boundary conditions for the pin fin ATEG used in automotive waste heat recovery are the Computational Fluid Dynamics (CFD) boundary and electric field boundary. The boundary settings for the model can be observed in Fig. 3. Initially, the ATEG is subjected to an ambient temperature of 303 K, and the convective heat transfer boundary condition is defined as:

$$-\lambda\frac{\partial T}{\partial n}=h_{nh}(T-T_{at}) \tag{21}$$

Here, h_{nh} represents the natural convective heat transfer coefficient, set at 15 W/(m^2·K) [42], and T_{at} denotes the ambient temperature.

The engine exhaust acts as the heat source and enters the heat exchanger with initial mass flow rates (m_a) ranging from 20 g/s to 40 g/s and initial temperatures (T_a) spanning from 473 K to 673 K. The implementation of this boundary condition is achieved by setting the velocity and temperature at the inlet surface of the fluid domain. The exhaust gas exits the heat exchanger at standard atmospheric pressure. Concerning the cooling system, the impact of water velocity on the TEG performance is found to be insignificant [46]. In the simulation, the radiator is supplied with cooling water at a velocity of 20 m/s and a temperature of 300 K. The temperature boundary conditions for the annular thermoelectric module are determined based on the temperature distribution obtained from CFD simulations. The lateral surfaces of the ATEM and the heat exchanger are adiabatic, while heat conduction occurs at the interface between the pipe wall and the ATEM.

Within the ATEM, thermocouples are connected in series to form a closed loop. One side of the load resistor and one terminal of the first thermocouple are grounded (with the voltage set to 0 V), and the other side of the load resistor is connected to one terminal of the last thermocouple.

2.4. Taguchi method

In engineering, the Design of Experiments (DOE) entails the identification of superior parameter combinations and the determination of the direction for further experiments aimed at achieving an optimized solution through the analysis and comparison of experimental results [47]. The Taguchi method provides significant advantages by reducing the number of required experiments through the use of orthogonal arrays while also facilitating the assessment of different factors' sensitivity. In the evaluation process, the Taguchi method employs signal-to-noise ratio (S/N) metrics, which are determined based on the mean and variance of the response. Target function analysis commonly employs three types of S/N ratios: "the larger the better," "the smaller

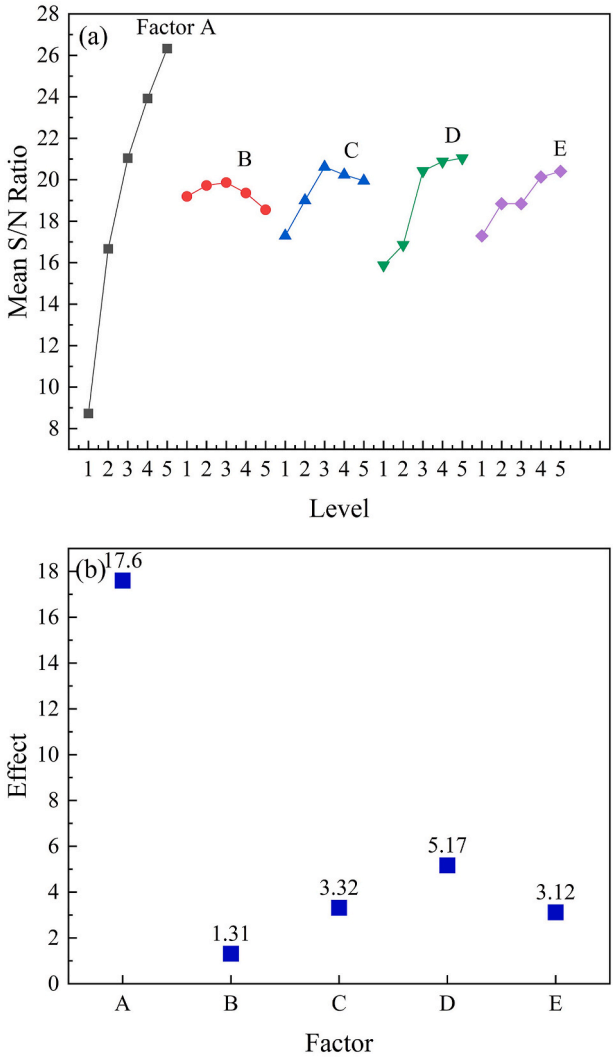

Fig. 11. (a) The average S/N ratio distribution and (b) the effect value of 5 factors on the net power.

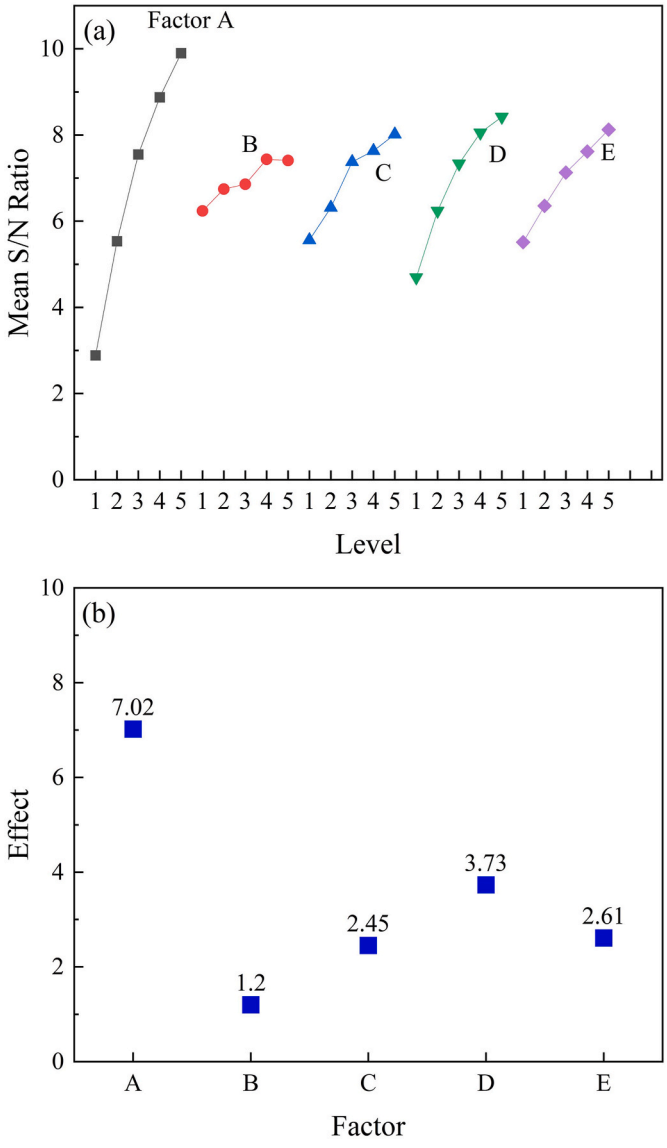

Fig. 12. (a) The average S/N ratio distribution and (b) the effect value of 5 factors on the net power.

the better," and "the nominal the better." In this study, the objective is to maximize the net power and efficiency, which falls under the "the larger the better" category. The S/N ratio for net power or efficiency is calculated as follows:

$$S/N = -10\log_{10}(1/f^2) \tag{22}$$

Where f is the value of P_{net} or η.

As shown in Table 3, the Taguchi method considers the output results of five factors: exhaust temperature, exhaust mass flow rate, fin height, fin diameter, and the number of fins, each at five different levels. The parameters of engine exhaust vary depending on the vehicle's operating conditions. In the case of a typical passenger car, the exhaust temperature fluctuates between 473 K and 673 K, while the mass flow rate of exhaust gas typically ranges from 20 g/s to 40 g/s [48]. When designing the heat dissipation pin fins and determining their geometric dimensions, we take into account the size range recommended by the work of Sertkaya et al. [49]. Fig. 4 illustrates the structural parameters of the pin fins, including the axial height (H) and the diameter (D) of a single cylindrical fin. Furthermore, we design and apply varying quantities of heat dissipation fins, ranging from 180 to 420, within the heat exchanger pipeline of the ATEG.

3. Model validation

3.1. Grid sensitivity

To solve the control equations mentioned above, the SIMPLEC algorithm within a pressure-velocity coupling solver is employed. The Least Squares Cell Based on the spatial discrete solution is selected. For solving momentum, turbulent kinetic energy, and turbulent dissipation rate, a second order upwind algorithm is applied. The summation of residuals is computed as follows:

$$Residualsum = \sum_{domain} \left|\alpha_{nb}\varnothing_{nb} + b - \alpha_p\varnothing_p\right| \tag{23}$$

Where α represents coefficient term, $\varnothing$ stands for the transient variable, and b represents the contribution of source terms. Convergence criteria for all residual values are set at 10^{-6}.

To assess grid independence, a grid sensitivity analysis is performed, with the temperature difference on the ATEM surface taken as the detection target. Typically, more accurate results are achieved with finer grid divisions, but they also necessitate longer computation times. Therefore, it is essential to determine an optimal grid size that ensures

Table 5
Comparison of the effect of different heat transfer enhancement methods.

Ref.	Thermoelectric generator shape	Working fluid		Hot fluid parameter		Heat transfer enhancement method	NPR
		Hot side	Cold side	T_a (K)	m_a (g/s)		
[21]	Plate-shaped	Air	Water	673	30	Intermediate heat transfer fluid	1.77
[35]	Annular	Air	Water	723	50	Concentric annular heat exchanger	1.65
[36]	Annular	Air	Water	673	30	Spiral tie	11.86
[59]	Plate-shaped	Air	Water	500	30	Convergent heat exchanger	3.02
[60]	Rectangular	Air	Air	353.15	30	Flat fin	2.05
[61]	Rectangular	Air	Water	603.15	28	Square pin fin	18.56
[62]	Plate-shaped	Air	Water	564.4	33.3	Porous medium embedding	1.44
[63]	Plate-shaped	Air	Water	551.2	22.86	Flow straightener	2.22
Present study	Annular	Air	Water	673	30	Circular pin fin	27.98

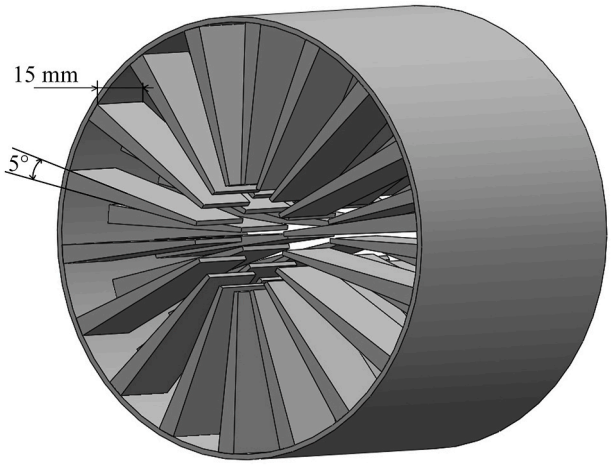

Fig. 13. Plate fin heat exchanger structure diagram.

effective results while maintaining a reasonable computation time. In the ATEG finite element model, as depicted in Fig. 5, a hexahedral grid is predominantly employed for grid partitioning, with the tetrahedral grid being utilized for irregular geometric areas. Additionally, a five-layer boundary layer network is established on the fluid surface in contact with the solid domain. Grid independence tests are performed on two separate systems: one without pin fins and another with pin fins integrated into the ATEG system.

Numerical simulations are performed on the smooth-tube air-to-water counterflow heat exchanger ATEG, without pin fins, using five different grid resolutions, as illustrated in Fig. 6(a): (i) 31,470, (ii) 566,881, (iii) 1,397,266, (iv) 3,357,511, and (v) 5,540,931. The results reveal a strong resemblance between simulations (iv) and (v), exhibiting an error of less than 1%. For the heat transfer channel equipped with 10 × 30 circular pin fins, measuring 2 mm in diameter and 20 mm in height, five different grid resolutions are employed, as shown in Fig. 6(b): (i) 774,911, (ii) 3,919,000, (iii) 48,944,980, (iv) 6,560,194, and (v) 9,813,946. The findings demonstrate an error of less than 1% between simulations (iv) and (v). It's worth noting that the computation time for grid (v) is approximately 4 h and 40 min, while grid (iv) requires 2 h and 50 min. Consequently, grid (iv) serves as a suitable compromise between computational accuracy and efficiency.

3.2. Validation of the finite element model

To validate the numerical accuracy of the model, a comparison is made between the simulation data and experimental results obtained from a relevant study in the literature conducted by Ref. [50]. They proposed a 3-D model for the TEM and established a corresponding testing system. In this study, a three-dimensional model of the same scale is constructed, and identical boundary conditions are applied, with $T_a = 450$ K and $T_c = 320.2$ K. By comparing the numerical data with the experimental results presented in Ref. [50], the impact of load resistance on the output power is investigated, as illustrated in Fig. 7. The findings indicate that the modeling approach employed in this study exhibits a maximum error of 1.08% when compared to the experimental data, demonstrating the model's effective reproduction of the experimental results.

To the best of the authors' knowledge, experimental data is currently lacking for the proposed pin fin ATEG structure in this study. In Ref. [51], an air-to-water thermoelectric generator was established, simulating steady inlet air temperature and mass flow rate using an air heater. Six serrated fins were incorporated in the heat exchanger to enhance heat exchange. To validate the accuracy of the conduction-convection simulation approach, the thermoelectric generator structure, boundary conditions, and solution of the control equations from Ref. [51] were reconstructed using the methods presented in this study. In Ref. [51], where the hot fluid inlet temperature was fixed at 550 K and the mass flow rate was set at 40 g/s, the output performance was tested under various load resistances. Although the structures differ, this allowed for the verification of the correctness of the numerical simulation approach in this study. Simulation results are compared with experimental data, as shown in Fig. 7(b). The numerical model yields a slightly higher output power than the experimental data, with a maximum error of 1.9%. From the perspective of simulating verification experiments, this deviation falls within an acceptable range. In summary, the obtained results align well with the literature, demonstrating the feasibility of the model.

3.3. Validation of the turbulence model

To validate the turbulence model, we refer to a study conducted by Selimefendigil et al. [52]. Fig. 7(c) presents a comparison between the Nusselt numbers obtained from our simulations at different Reynolds numbers ranging from 6505 to 32593 and the corresponding data from the literature. The results of the model show an average error of less than 5% when compared to the literature data, indicating the effectiveness of the numerical model.

4. Results and discussion

4.1. Thermoelectric performance of the pin fin ATEG

4.1.1. Pin ATEG power generation characteristics

To assess the impact of incorporating pin fins in a circular pipe on the thermoelectric characteristic of the ATEG, Fig. 8 presents the voltage distribution, current distribution, heat exchanger temperature distribution, and hot-side temperature distribution of the ATEG under the conditions of $T_a = 523$ K and $m_a = 25$ g/s. Fig. 8(a) displays the temperature distribution in a smooth pipe without pin fins, showing a significant temperature decrease from the inlet to the outlet. The hot-side temperature of the ATEM reaches only 354 K, with a maximum operating temperature difference of approximately 50 K. In contrast, Fig. 8

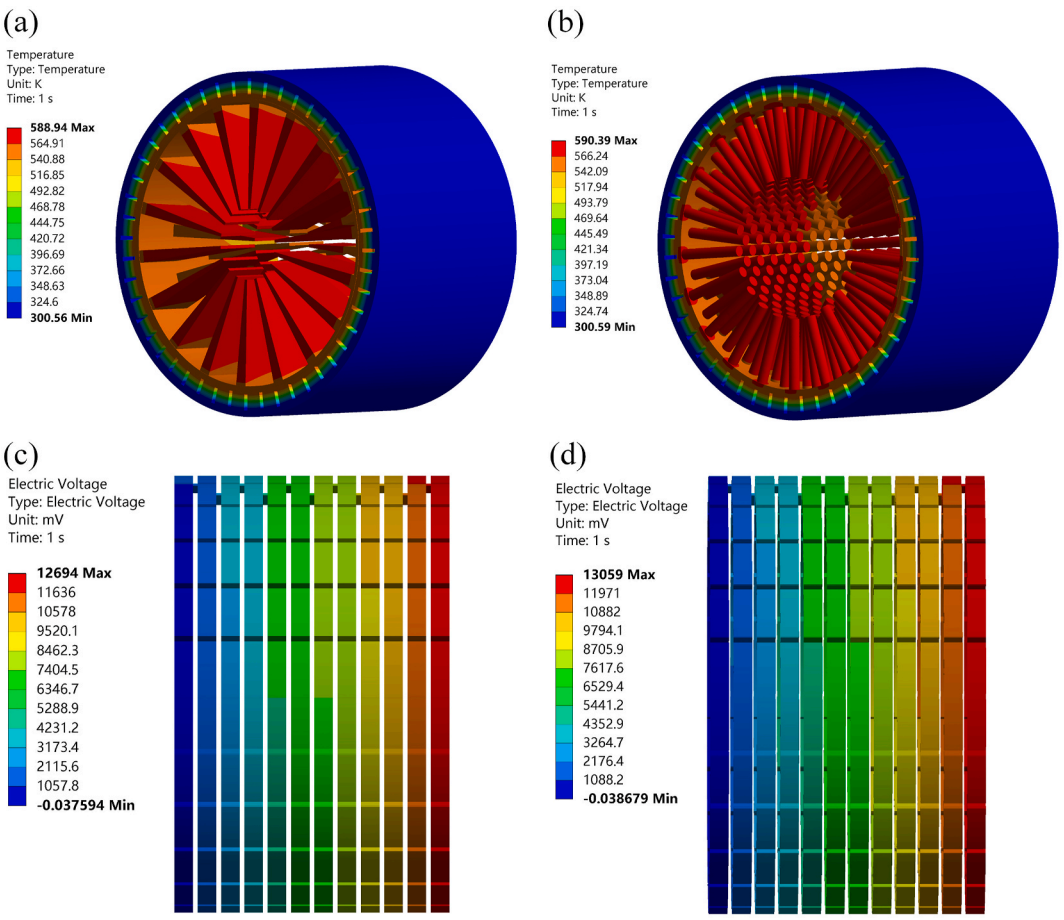

Fig. 14. Numerical results of ATEG at $T_a = 673$ K and $m_a = 30$ g/s. (a) Temperature distribution of plate fin ATEG, (b) temperature distribution of pin fin ATEG, (c) voltage distribution of plate fin ATEG, and (d) voltage distribution of pin fin ATEG.

(c) illustrates the ATEG equipped with 10 × 18 pin fins, each measuring 3 mm in diameter and 20 mm in height. This configuration achieves a hot-side temperature of 432 K, with the temperature difference between the two ends of the ATEM reaching up to 128.59 K.

Furthermore, in the smooth pipe, the temperature difference between the hot fluid and the heat exchanger wall is approximately 169 K. However, in the pin-finned ATEG, this temperature difference decreases significantly to only 91 K. Additionally, the temperature difference between the inlet and outlet of the pin-finned ATEG is considerably greater than that in the smooth pipe. This indicates that the introduction of pin fins enhances the extraction of thermal energy. Similar to square pin fins [53], circular pin fins contribute to fluid disturbance, increase the heat transfer area, and improve heat transfer efficiency. Both structures exhibit similar characteristics in terms of the distribution of cold-side temperatures. Therefore, the pin-finned heat exchanger configuration can amplify the temperature difference of the ATEM, resulting in a higher output voltage generation.

Fig. 8(b) and (d) display the potential distribution of the ATEM in smooth and pin-fin-inserted heat exchangers, respectively. The ATEG output voltage for the smooth pipe is 2.469 V, while the pin-fin-inserted pipe achieves a higher output voltage of 6.490 V. When connecting a resistor with a resistivity of 0.0125 Ω m at the load end and performing a simple calculation, it is determined that the output power increases from 1.219 W to 8.425 W, resulting in a significant 5.9-fold improvement. This finding aligns with the conclusion drawn by Jiang et al. [54], who observed that TEG modules with fins can achieve dozens of times higher output power. The distribution of current density in the ATEM is presented in Fig. 7(f), where the conductivity of the material primarily influences the current density. As a result, the maximum current density is observed along the direction of the copper wire.

4.1.2. *Thermal and electrical impedance matching*

Studies have indicated that in TEG systems, the load resistance required for achieving peak power output is generally higher than the internal resistance. This is primarily due to the mismatch between thermal resistance and electrical resistance [55]. Therefore, it is not accurate to assume that maximum power output is achieved when the internal and external loads are equal. Additionally, the internal resistance of the ATEG varies with changes in operating conditions due to the temperature-dependent characteristic of thermoelectric semiconductor [56]. To investigate the optimal thermoelectric performance of the pin fin ATEG, impedance matching is conducted. Fig. 9 illustrates how the output power of the pin fin ATEG is influenced by the load resistance under various exhaust mass flow rates and temperatures. As the load resistance is raised, the output power exhibits an initial increase followed by a subsequent decrease. Increasing the mass flow rate leads to a corresponding increase in the output power, although this effect becomes less pronounced with further increments in the mass flow rate. In contrast, the exhaust temperature plays a crucial role in determining the output power, as it demonstrates a positive correlation with power output, corroborating the findings of Zhu et al. [57]. It is evident from the figure that regardless of changes in operating conditions, the optimal load resistance for ATEM is approximately 5 Ω. Consequently, a load resistance of 5 Ω is employed in the subsequent numerical simulations.

4.1.3. *Influence of pin fin structure on thermoelectric performance*

As pointed out by Chen et al. [53], increasing the number of rectangular fins leads to a higher heat transfer rate. This conclusion can also

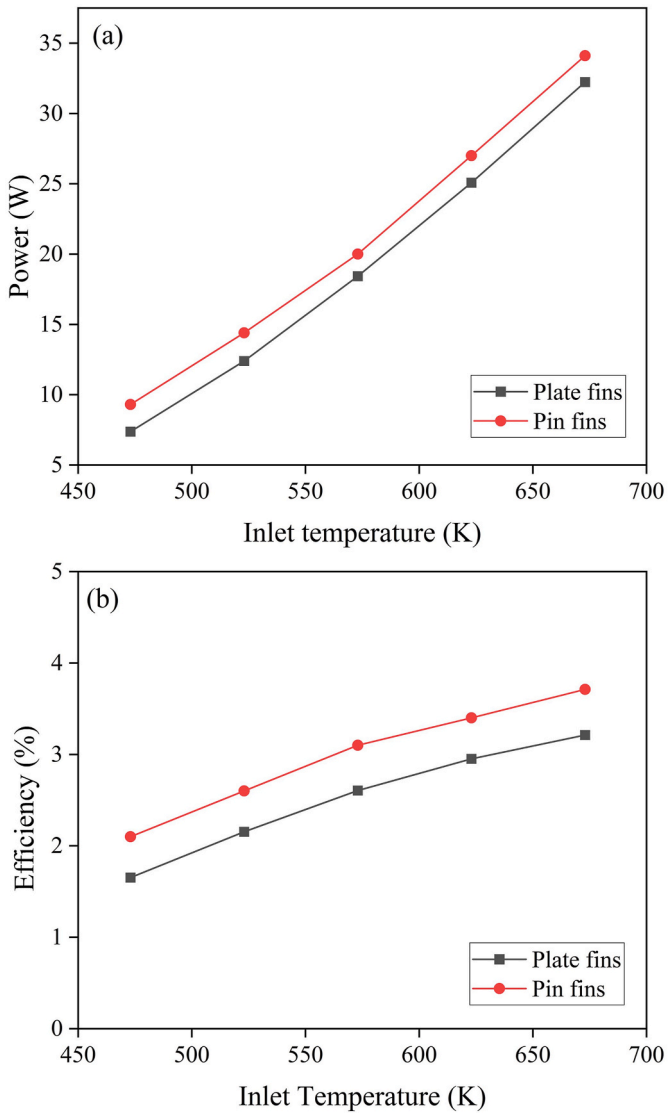

Fig. 15. The influence of the exhaust temperature T_a on the (a) power output and (b) conversion efficiency of the two types of ATEGs under $m_a = 30$ g/s.

be applied to circular pin fin ATEGs. However, the impact of the structural parameters of circular pin fins on the performance of ATEGs has yet to be determined. In the hot-side channel of the ATEG, we install 10 × 30 pin fins with various specifications. The fin diameter, D, is set to 1, 1.5, 2, 2.5, and 3, while the fin height, H, is set to 10, 15, 20, 25, and 30. Fig. 10 depicts the effects of these pin fin structural parameters on the ATEG's power output, efficiency, net power, and pressure drop.

Based on the data presented in Fig. 9(a) and (b), it becomes clear that increasing the diameter and height of the pin fins results in a noticeable enhancement in both output power and efficiency. Augmenting both the height and diameter leads to a more pronounced disturbance in the fluid region, thereby increasing convective heat transfer effects. Simultaneously, the enlarged surface area of the pin fins in contact with the hot fluid, along with the efficient thermal conductivity of the metal pins, elevates the heat exchanger wall temperature. This increases the temperature difference of the thermoelectric module, thereby enhancing the output power and conversion efficiency.

Nevertheless, it is crucial to take into account the possible drawbacks associated with intensified fluid disruption in the automotive exhaust system, such as the potential loss of engine pumping power due to elevated exhaust back pressure [58]. Fig. 9(c) and (d) examine the influence of pin fin structural parameters on the net power and exhaust pressure drop of the ATEG system. The results demonstrate that, for different values of H, the net power (P_{net}) increases with increasing D. However, P_{net} initially increases and then decreases with increasing H, particularly for larger pin fin diameters. A preliminary observation at different D values suggests an optimal pin fin height of $H = 20$ mm. The change in net power trend is closely related to Fig. 10(d), which illustrates that the heat exchanger pressure drop rises with increasing pin fin diameter and height. The fluid disturbance caused by the pin fins increases the fluid pressure drop within the heat exchanger. When the negative effects of increased pin fin volume and heat transfer area outweigh the benefits of increased heat transfer rate, the net power starts to decrease.

4.2. Optimal design based on Taguchi method

Taking into account all possible scenarios, a total of 5^5 (3125) simulation calculations are required to capture the changing trends under various conditions. This process is highly time-consuming, typically taking several months to complete due to the complex nature of the established three-dimensional high-fidelity numerical model. To investigate the effects of operational conditions and pin fin parameters on ATEG performance, a 25 orthogonal experiment with 5 factors and 5 levels is conducted in the simulation. This experiment aims to determine the impact and sensitivity of each factor on the thermal-electric performance of pin fin ATEGs and identify the optimal combination of conditions while saving significant time and resources.

Table 4 presents the simulation results of net power and efficiency for the 25 orthogonal experiments, along with their corresponding S/N ratios. Among these experiments, run23 achieves the highest net power of 28.736 W, while the lowest result is obtained in run5 with −3.177 W Run23 also demonstrates the maximum efficiency of 3.590%, whereas run1 exhibits the minimum efficiency of 0.681%. These results indicate that the performance of the ATEG is greatly influenced by five different factors.

The average S/N ratio for each factor in relation to net power or efficiency serves as an indicator of the factor's contribution. For example, for net power, the average signal-to-noise ratio of level 1 factor A is calculated as (0.784 + 8.049+12.956 + 11.833+10.037)/5 = 8.73171574. Similarly, the average signal-to-noise ratio values for other factors and specific levels are calculated. Fig. 11(a) illustrates the average S/N ratio corresponding to the net power of the five factors, while Fig. 11(b) displays the effect value of the five factors on the net power. The effect value is obtained by subtracting the minimum average S/N ratio from the maximum S/N ratio. A higher effect value indicates a more significant influence of the corresponding factor on the net power. As depicted in Fig. 11(b), factor A, representing the exhaust temperature, exhibits a substantial effect value of 17.6 on the net power, surpassing the other factors by a significant margin. This observation aligns with the results of Luo et al. [59]. Conversely, the minimum value of factor B suggests that altering the mass flow rate has a relatively minor effect on the net power, as increasing the mass flow rate leads to simultaneous increases in both the output power and pumping power.

The ranking of the five factors influencing net power is as follows: A > D > C > E > B. The net output power exhibits an initial increase followed by a decrease as the pin fin height is raised, in accordance with the observations depicted in Fig. 9. Moreover, it demonstrates an upward trend of net power as the pin fin diameter is enlarged, aligning with the aforementioned findings. Furthermore, the influence of pin fin diameter on net power outweighs that of height, whereas the impact of pin fin quantity and height on net power is roughly equivalent.

Fig. 12(a) illustrates the average S/N ratio corresponding to the conversion efficiency of the five factors. The average S/N ratio demonstrates a consistent increase as the levels of all factors rise. This can be attributed to the calculation of efficiency, which relies on the output power. By increasing the levels of all factors, the heat transfer rate and working temperature difference of the ATEM are enhanced,

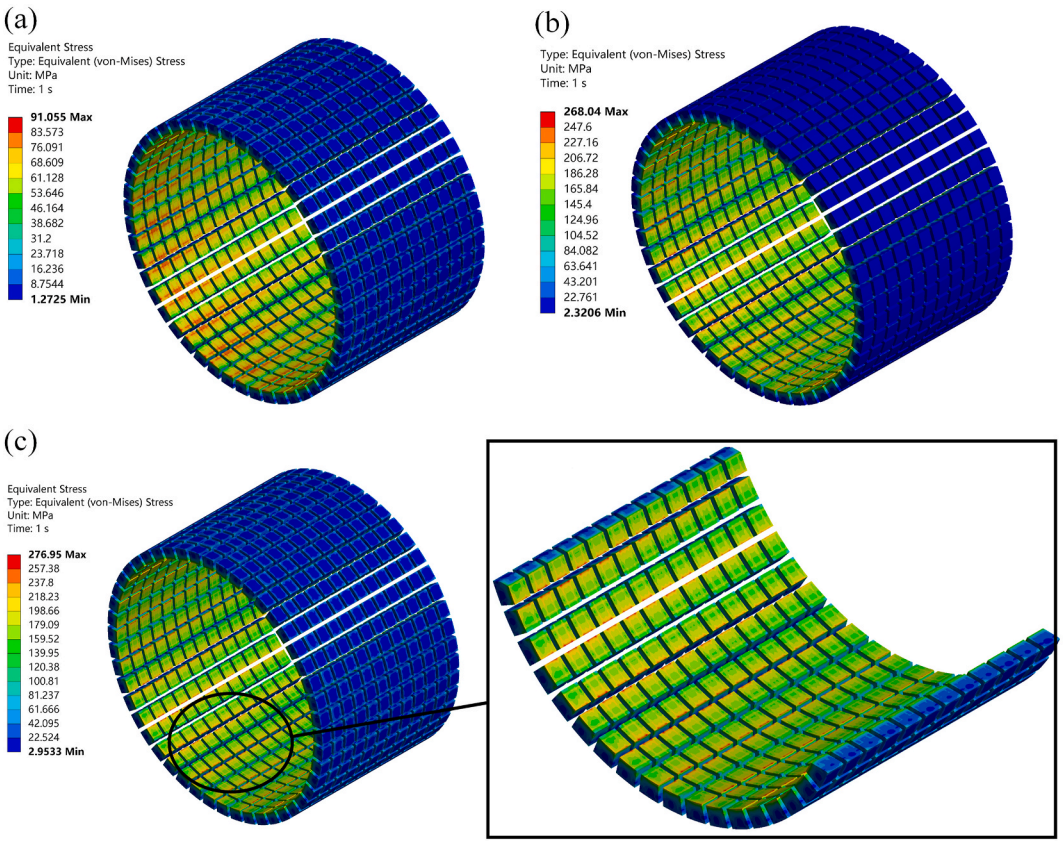

Fig. 16. Thermal stress distributions on the PN legs of (a) smooth pipe ATEG, (b) plate fin ATEG, and (c) pin fin ATEG at $m_a = 30$ g/s and $T_a = 673$ K.

subsequently resulting in an overall boost in the output power. Fig. 12 (b) shows the effect value of the five factors on the conversion efficiency. It can be seen that the impact of the five factors on efficiency and net output power are in the same order. Moreover, the trend of the impact of factors C and D on efficiency is consistent with that shown in Fig. 9.

To determine the ideal combination of factors A-E for the ATEG, an analysis of the average signal-to-noise ratio curve is conducted. Upon examining Fig. 12(a), it becomes evident that the combination A5B3C3D5E5 exhibits the highest signal-to-noise ratio, signifying optimal performance for the ATEG. This particular combination corresponds to an inlet temperature of 673 K, a mass flow rate of 30 g/s, a fin height of 20 mm, a fin diameter of 3 mm, and a total of 480 fins. Notably, this specific combination is not included in the 25 experiments documented in Table 4. By setting the parameters to the optimal combination and performing an additional numerical calculation, it is found that the maximum net power reaches 34.11 W, which is 18.7% higher than the maximum value obtained in the 25 experiments in Table 4. These results demonstrate that the Taguchi method effectively improves the performance of the pin fin ATEG while reducing time costs.

To compare the enhanced heat transfer effect proposed in this study with other methods, introduce the Net Power Ratio (NPR) [64]. The NPR represents the ratio of the TEG net power after applying the enhanced heat transfer measures to the net power before applying these measures:

$$NPR = \frac{P_{net}}{P_{net0}} \tag{24}$$

Where P_{net0} represents the net power when TEGs are arranged outside smooth pipes, while P_{net} represents the net power after applying enhanced heat transfer measures. The NPR metric takes into account both the positive and negative effects of enhanced heat transfer measures on TEG system performance, making it useful for evaluating the overall performance of such measures.

Table 5 provides a comparison of the NPR for various heat transfer enhancement methods. To the best of our knowledge, this method is considered to exhibit superior overall performance compared to other reported TEG heat transfer enhancement methods, highlighting the effectiveness of our design and the potential practicality of the pin-fin ATEG.

4.3. Comparative study

Finned plates have gained popularity as an effective solution for improving the heat transfer efficiency of conventional flat plate thermoelectric generators. They offer the advantage of easy integration with plate-type heat exchangers and direct installation onto TEMs. Consequently, there has been extensive research conducted on the application of finned plates [65]. In this section, we aim to compare the effectiveness and thermomechanical property of plate fins and circular pin fins in enhancing the performance of an ATEG.

A plate fin design suitable for annular pipes is developed based on the optimal operating combination of a pin fin ATEG, as shown in Fig. 13. The designed fin configuration consists of 18 × 4 fins with a length of 15 mm and an axial angle of 5°. To ensure a fair comparison, the total volume of the plate fin structure remains the same as that of the pin fin ATEG under optimal parameters, with all other boundary conditions being identical. Fig. 14 illustrates the temperature and voltage distributions of the plate fin ATEG and the pin fin ATEG under $T_a = 673$ K and $m_a = 30$ g/s. It can be observed that the maximum temperatures of the two ATEGs are almost identical. The plate fin ATEG achieves an output power of 32.23 W, while the pin fin heat exchanger attains 34.11 W, resulting in a 5.83% increase compared to the plate fin ATEG. Furthermore, the pin fin heat exchanger exhibits a significantly smaller pressure drop than the plate fin heat exchanger, indicating a reduced negative impact on the engine. Fig. 15 shows the influence of the inlet temperature T_a on the output power and efficiency of the two types of fin

heat exchangers under $m_a = 30$ g/s. It can be seen that the pin fin ATEG consistently outperforms the plate fin ATEG in terms of output power and efficiency across various boundary conditions.

To investigate the effect of renovating the hot-end heat exchanger on the thermomechanical performance of the ATEM, we analyze the thermal stress distribution on the ATEM. Fig. 16 shows the thermal stress distribution on the ATEM under different heat exchanger structures at $m_a = 30$ g/s and $T_a = 673$ K. For these two heat exchanger configurations, the maximum thermal stress on the legs occurs at the edge of the PN leg due to stress concentration at locations with large temperature gradients and structural discontinuities. Fig. 16(a) illustrates the thermal stress distribution of the ATEG using a smooth pipe. It is observed that the thermal stress on the hot side of the ATEC is significantly higher than that on the cold side, and the maximum thermal stress on the leg is 91.055 MPa. Fig. 16(b) shows the ATEM thermal stress distribution after installing plate fins in the annular pipe. Fig. 16(c) displays the thermal stress distribution of the pin fin ATEG using the optimal parameter combination of the pin fin determined in the previous section. In the pin fin ATEG, the maximum thermal stress on the PN leg is 276.95 MPa, which is 204.16% higher than before installing the fins. The maximum thermal stress in the pin fin ATEG increases by 4.82% compared to the plate fin ATEG. In this scenario, the primary factor influencing thermal stress on the ATEM is the temperature distribution along the thermoelectric legs. This is because, compared to flat-fin ATEMs, the wall temperature and thermoelectric leg temperatures are significantly elevated in pin-fin ATEG.

In the current study, the most likely locations for fractures are the contact area between the hot-end surface of the PN legs and the solder, as well as the edge of the PN legs. It is important to note that the comparison between pin fins and plate fins in this section is specific to certain conditions, and further investigation is needed to examine the enhanced heat transfer effect of pin fins and plate fins under different operating conditions.

5. Conclusions

To enhance heat transfer and improve the thermoelectric performance of thermoelectric generators used for waste heat recovery from automobile exhaust gas, a design featuring an annular thermoelectric generator with circular pin fins has been developed. This design incorporates a fin heat exchanger that is specifically adapted to the automobile exhaust pipe. A three-dimensional numerical simulation method is employed to analyze the heat transfer characteristics, thermoelectric performance, and thermomechanical performance of two types of annular thermoelectric generators: those with circular pin fins and those with plate fins. To determine the optimal design parameters, considering five factors at five levels, the Taguchi method is employed using an L_{25} orthogonal matrix. The study evaluates the sensitivity of these selected parameters to the thermoelectric performance. Additionally, the impact of introducing plate fins or pin fins in an annular heat exchanger on the thermoelectric performance and the thermal stress on the PN legs is investigated. Based on the comprehensive findings of this investigation, the following conclusions can be drawn:

1. A 3-D coupled multiphysical model is established to simultaneously consider fluid flow, conjugate heat transfer, and thermoelectric effects, providing accurate predictions of the thermoelectric and thermomechanical performance. This comprehensive model determines the output characteristics and generates corresponding profiles, including temperature distribution, voltage distribution, current density distribution, and thermal stress distribution.
2. The size of pin fins significantly impacts thermoelectric performance. Increasing both the diameter and height of pin fins improves output power and efficiency. However, increasing pin fin height results in a significant increase in pipeline pressure drop, leading to an initial net power increase followed by a subsequent decrease.
3. The influence of the five design parameters on net power and efficiency can be ranked as follows: hot gas temperature > hot gas mass flow rate > pin fin height > pin fin diameter > number of pin fins. The optimal values for these parameters are 673 K, 30 g/s, 20 mm, 3 mm, and 10 × 42, respectively.
4. With the optimal parameter combination determined by the Taguchi method, a maximum net output power of 34.11 W is achieved, representing an 18.7% improvement compared to the maximum value obtained in the 25 orthogonal experiments.
5. A comparative study between the installation of plate fins and circular pin fins in a ring-shaped heat exchanger reveals that the pin fin thermoelectric generator exhibits a 5.83% increase in output power and a 4.82% increase in maximum thermal stress on the PN legs compared to the traditional plate fin thermoelectric generator when the same volume of fins is utilized.

CRediT authorship contribution statement

Wenlong Yang: Data curation, Investigation, Methodology, Writing – review & editing. **Chenchen Jin:** Data curation, Investigation, Methodology, Software. **Wenchao Zhu:** Data curation, Investigation, Methodology. **Yang Li:** Conceptualization, Validation, Writing – review. **Rui Zhang:** Project administration, Supervision, Writing – review. **Liang Huang:** Funding acquisition, Writing – review. **Changjun Xie:** Conceptualization, Funding acquisition, Project administration, Supervision, Writing – review & editing. **Ying Shi:** Conceptualization, Project administration, Writing – review.

Declaration of competing interest

The authors declare that they have no known competing financial interests or personal relationships that could have appeared to influence the work reported in this paper.

Acknowledgments

This research was funded by the National Natural Science Foundation of China (51977164).

References

[1] D.V. Singh, E. Pedersen, A review of waste heat recovery technologies for maritime applications, Energy Convers. Manag. 111 (2016) 315–328.
[2] J. Yang, F.R. Stabler, Automotive applications of thermoelectric materials, J. Electron. Mater. 38 (2009) 1245–1251.
[3] N.V. Burnete, F. Mariasiu, C. Depcik, I. Barabas, D. Moldvanu, Review of thermoelectric generation for internal combustion engine waste heat recovery, Prog. Energ. Combust. 91 (2022), 101009.
[4] S. Lan, Q. Li, X. Guo, S. Wang, R. Chen, Fuel saving potential analysis of bifunctional vehicular waste heat recovery system using thermoelectric generator and organic Rankine cycle, Energy 263 (2023), 125717.
[5] C. Gong, X. Si, F. Liu, Combined effects of excess air ratio and EGR rate on combustion and emissions behaviors of a GDI engine with CO2 as simulated EGR (CO2) at low load, Fuel 293 (2021), 120442.
[6] H. He, F. Sun, Z. Wang, C. Lin, C. Zhang, R. Xiong, J. Deng, X. Zhu, P. Xie, S. Zhang, Z. Wei, W. Cao, L. Zhai, China's battery electric vehicles lead the world: achievements in technology system architecture and technological breakthroughs, Green Energy Intellig. Transport. 1 (2023), 100020.
[7] C. Gong, X. Si, F. Liu, Combined effects of excess air ratio and EGR rate on combustion and emissions behaviors of a GDI engine with CO_2 as simulated EGR (CO_2) at low load, Fuel 293 (2021), 120442.
[8] D.C. Rakopoulos, C.D. Rakopoulos, E.G. Giakoumis, Impact of properties of vegetable oil, bio-diesel, ethanol and n-butanol on the combustion and emissions of turbocharged HDDI diesel engine operating under steady and transient conditions, Fuel 156 (2015) 1–19.
[9] L. Zhu, H. Li, S. Chen, X. Tian, X. Kang, X. Jiang, S. Qiu, Optimization analysis of a segmented thermoelectric generator based on genetic algorithm, Renew. Energy 156 (2020) 710–718.
[10] A.S. Easa, R.A. Khalaf-Allah, A.A. Al-Nagdy, M.T. Tolan, S.M. Mohamed, Experimental study of saving energy and improving Stirling water dispenser performance using the waste heat of both pistons friction, Appl. Therm. Eng. 213 (2022), 118727.

[11] X. Liu, Y.D. Deng, Z. Li, C.Q. Su, Performance analysis of a waste heat recovery thermoelectric generation system for automotive application, Energy Convers. Manag. 90 (2015) 121–127.
[12] M. Rakshit, D. Jana, D. Banerjee, General strategies to improve thermoelectric performance with an emphasis on tin and germanium chalcogenides as thermoelectric materials, J. Mater. Chem. A 10 (2022) 6872–6926.
[13] L. Zhu, H. Li, S. Chen, X. Tian, X. Kang, X. Jiang, S. Qiu, Optimization analysis of a segmented thermoelectric generator based on genetic algorithm, Renew. Energy 156 (2020) 710–718.
[14] Y. Ge, K. He, L. Xiao, W. Yuan, S. Huang, Geometric optimization for the thermoelectric generator with variable cross-section legs by coupling finite element method and optimization algorithm, Renew. Energy 183 (2022) 294–303.
[15] Y. Luo, L. Li, Y. Chen, C.N. Kim, Influence of geometric parameter and contact resistances on the thermal-electric behavior of a segmented TEG, Energy 254 (2022), 124487.
[16] M.H. Zaher, M.Y. Abdelsalam, J.S. Cotton, Non-dimensional design optimization of annular thermoelectric generators integrated in waste heat recovery applications, Energy Convers. Manag. 253 (2022), 115141.
[17] Z.G. Shen, S.Y. Wu, L. Xiao, Theoretical analysis on the performance of annular thermoelectric couple, Energy Convers. Manag. 89 (2015) 244–250.
[18] W. Yang, W. Zhu, Y. Li, C. Xie, B. Xiong, Y. Shi, W. Lin, Global structural optimization of annular thermoelectric generators based on a dual-finite-element multiphysical model, Appl. Therm. Eng. 220 (2023), 119797.
[19] T.Y. Kim, J. Kwak, B.W. Kim, Energy harvesting performance of hexagonal shaped thermoelectric generator for passenger vehicle applications: an experimental approach, Energy Convers. Manag. 160 (2018) 14–21.
[20] F. Selimefendigil, H.F. Oztop, Optimization assisted CFD for using double porous cylinders on the performance improvement of TEG mounted 3D channels, Sustain. Energy Technol. Assess. 52 (2022), 102303.
[21] Y. Zhao, M. Lu, Y. Li, M. Ge, L. Xie, L. Liu, Characteristics analysis of an exhaust thermoelectric generator system with heat transfer fluid circulation, Appl. Energy 304 (2021), 117896.
[22] W. Yang, W. Zhu, B. Du, H. Wang, L. Xu, C. Xie, Y. Shi, Power generation of annular thermoelectric generator with silicone polymer thermal conductive oil applied in automotive waste heat recovery, Energy 282 (2023), 128400.
[23] R.A. Khalaf-Allah, E.I. Eid, A.E.H.A. Ellithy, A.S. Easa, Experimental investigation of the influence of modifying the inner tube outer surface on free convection in A concentrated double pipe, Exp. Heat Transf. (2022).
[24] A.S. Easa, R.A. Khalaf-Allah, S.M. Mohamed, M.I.A. Habba, M.T. Tolan, Optimization of humidification-dehumidification solar desalination unit: comparative analysis, Appl. Therm. Eng. 236 (2023), 121610.
[25] E. Youse, A.A. Nejad, A. Rezania, Higher power output in thermoelectric generator integrated with phase change material and metal foams under transient boundary condition, Energy 256 (2022), 124644.
[26] D.R. Karana, R.R. Sahoo, Thermohydraulic performance of a new internal twisted ribs automobile exhaust heat exchanger for waste heat recovery applications, Int. J. Energy Res. 44 (2020) 11417–11433.
[27] H. Usman, H.M. Ali, A. Arshad, M.J. Ashraf, S. Khushnood, M.M. Janjua, S.N. Kazi, An experimental study of PCM based finned and un-finned heat sinks for passive cooling of electronics, Heat Mass Transf 54 (2018) 3587–3598.
[28] Y.L. He, H. Han, W.Q. Tao, Y.W. Zhang, Numerical study of heat-transfer enhancement by punched winglet-type vortex generator arrays in fin-and-tube heat exchangers, Int. J. Heat Mass Transf. 55 (2012) 5449–5458.
[29] D. Luo, R. Wang, Y. Yan, W. Yu, W. Zhou, Transient numerical modelling of a thermoelectric generator system used for automotive exhaust waste heat recovery, Appl. Energy 297 (2021), 117151.
[30] X. Lu, X. Yu, Z. Qu, Q. Wang, T. Ma, Experimental investigation on thermoelectric generator with non-uniform hot-side heat exchanger for waste heat recovery, Energy Convers. Manag. 150 (2017) 403–414.
[31] A.S. Easa, W.M. El-Maghlany, M.M. Hassan, M.T. Tolan, The performance of a gamma-type stirling water dispenser with twin wavy plate heat exchangers, Case Stud. Therm. Eng. 39 (2022), 102464.
[32] D. Luo, Z. Liu, Y. Yan, Y. Li, R. Wang, L. Zhang, X. Yang, Recent advances in modeling and simulation of thermoelectric power generation, Energy Convers. Manag. 273 (2022), 116389.
[33] M. Zhang, J. Wang, Y. Tian, Y. Zhou, J. Zhang, H. Xie, Z. Wu, W. Li, Y. Wang, Performance comparison of annular and flat-plate thermoelectric generators for cylindrical hot source, Energy Rep. 7 (2021) 413–420.
[34] S. Shittu, G. Li, X. Zhao, X. Ma, Review of thermoelectric geometry and structure optimization for performance enhancement, Appl. Energy 268 (2020), 115075.
[35] W. Yang, W. Zhu, Y. Li, L. Zhang, B. Zhao, C. Xie, Y. Yan, L. Huang, Annular thermoelectric generator performance optimization analysis based on concentric annular heat exchanger, Energy 239 (2022), 122127.
[36] W. Zhu, A. Xu, W. Yang, B. Xiong, C. Xie, Y. Li, L. Xu, Y. Shi, W. Lin, Optimal design of annular thermoelectric generator with twisted tape for performance enhancement, Energy Convers. Manag. 270 (2022), 116258.
[37] A.S. Easa, S.M. Mohamed, W.S. Barakat, M.I.A. Habba, M.G. Kandel, R.A. Khalaf-Allah, Water production from a solar desalination system utilizing a high-speed rotary humidifier, Appl. Therm. Eng. 224 (2023), 120150.
[38] T. Saravanakumar, D.S. Kumar, Heat transfer study on different surface textured pin fin heat sink, Int. Commun. Heat Mass Transf. 119 (2020), 104902.
[39] G. Sung, D.-Y. Na, S.-J. Yook, Enhancement of the cooling performance of a pin fin heat sink based on the chimney effect using aluminum tape, Int. J. Heat Mass Transf. 201 (2023), 123613.
[40] M. Abdelgaied, A.E. Kabeel, A Performance improvement of pyramid solar distillers using a novel combination of absorber surface coated with CuO nano black paint, reflective mirrors, and PCM with pin fins, Renew. Energy 180 (2021) 494–510.
[41] W. He, S. Wang, C. Lu, X. Zhang, Y. Li, Influence of different cooling methods on thermoelectric performance of an engine exhaust gas waste heat recovery system, Appl. Energy 162 (2016) 1251–1258.
[42] D. Luo, R. Wang, Y. Yan, Z. Sun, W. Zhou, R. Ding, Comparison of different fluid-thermal-electric multiphysics modeling approaches for thermoelectric generator systems, Renew. Energy 180 (2021) 1266–1277.
[43] D. Luo, R. Wang, Y. Yan, W. Yu, W. Zhou, Transient numerical modelling of a thermoelectric generator system used for automotive exhaust waste heat recovery, Appl. Energy 297 (2021), 117151.
[44] D. Luo, Y. Yan, R. Wang, W. Zhou, Numerical investigation on the dynamic response characteristics of a thermoelectric generator module under transient temperature excitations, Renew. Energy 170 (2021) 811–823.
[45] Y. Ootao, Y. Tanigawa, Three-dimensional solution for transient thermal stresses of functionally graded rectangular plate due to nonuniform heat supply, Int. J. Mech. Sci. 47 (2005) 1769–1788.
[46] W.-H. Chen, C.-Y. Liao, C.-I. Hung, W.-L. Huang, Experimental study on thermoelectric modules for power generation at various operating conditions, Energy 45 (2012) 874–881.
[47] A.S. Easa, R.A. Khalaf-Allah, S.M. Mohamed, M.G. Kandel, W.S. Barakat, M.I. A. Habba, Experimental and statistical analysis of a solar desalination HDH arrangement with high-speed acceleration centrifugal sprayer, Desalination 551 (2023), 116419.
[48] D. Luo, Z. Sun, R. Wang, Performance investigation of a thermoelectric generator system applied in automobile exhaust waste heat recovery, Energy 238 (2022), 121816.
[49] A.A. Sertkaya, M. Ozdemir, E. Canli, Effects of pin fin height, spacing and orientation to natural convection heat transfer for inline pin fin and plate heat sinks by experimental investigation, Int. J. Heat Mass Transf. 177 (2021), 121527.
[50] D. Luo, R. Wang, W. Yu, W. Zhou, Parametric study of a thermoelectric module used for both power generation and cooling, Renew. Energy 154 (2020) 542–552.
[51] D. Luo, R. Wang, W. Yu, W. Zhou, Performance evaluation of a novel thermoelectric module with BiSbTeSebased material, Appl. Energy 238 (2019) 1299–1311.
[52] F. Selimefendigil, H.F. Oztop, R. Ozgul, Turbulent forced convection of nanofluid in an elliptic cross-sectional pipe, Int. Commun. Heat Mass Transf. 109 (2019), 104384.
[53] W.-H. Chen, C.-M. Wang, D.-S. Lee, E.E. Kwon, V. Ashokkumar, A.B. Culaba, Optimization design by evolutionary computation for minimizing thermal stress of a thermoelectric generator with varied numbers of square pin fins, Appl. Energy 314 (2022), 118995.
[54] J.-Y. Jang, Y.-C. Tsai, C.-W. Wu, A study of 3-D numerical simulation and comparison with experimental results on turbulent flow of venting flue gas using thermoelectric generator modules and plate fin heat sink, Energy 53 (2013) 270–281.
[55] Z.-Z. He, A coupled electrical-thermal impedance matching model for design optimization of thermoelectric generator, Appl. Energy 269 (2020), 115037.
[56] W. Zhu, Z. Weng, Y. Li, L. Zhang, B. Zhao, C. Xie, Y. Shi, L. Huang, Y. Yan, Theoretical analysis of shape factor on performance of annular thermoelectric generators under different thermal boundary conditions, Energy 239 (2022), 122285.
[57] W. Zhu, W. Yang, Y. Yang, Y. Li, H. Li, Y. Shi, Y. Yan, C. Xie, Economic configuration optimization of onboard annual thermoelectric generators under multiple operating conditions, Renew. Energy 197 (2022) 486–499.
[58] D. Luo, Z. Wu, Y. Yan, D. Ji, Z. Cheng, R. Wang, Y. Li, X. Yang, Optimal design of a heat exchanger for automotive thermoelectric generator systems applied to a passenger car, Appl. Therm. Eng. 227 (2023), 120360.
[59] D. Luo, R. Wang, W. Yu, W. Zhou, A numerical study on the performance of a converging thermoelectric generator system used for waste heat recovery, Appl. Energy 270 (2020), 115181.
[60] W.-H. Chen, Y.-B. Chiou, R.-Y. Chein, J.-Y. Uan, X.-D. Wang, Power generation of thermoelectric generator with plate fins for recovering low-temperature waste heat, Appl. Energy 306 (2022), 118012.
[61] W.-H. Chen, C.-M. Wang, L.H. Saw, A.T. Hoang, A.A. Bandala, Performance evaluation and improvement of thermoelectric generators (TEG): fin installation and compromise optimization Energ, Convers. Manag. 250 (2021), 114858.
[62] Y. Choi, A. Negash, T.Y. Kim, Waste heat recovery of diesel engine using porous medium-assisted thermoelectric generator equipped with customized thermoelectric modules, Energy Convers. Manag. 197 (2019), 111902.
[63] A.A. Negash, Y. Choi, T.Y. Kim, Experimental investigation of optimal location of flow straightener from the aspects of power output and pressure drop characteristics of a thermoelectric generator, Energy 219 (2021), 119565.
[64] Y. Yang, S. Wang, Y. Zhu, Evaluation method for assessing heat transfer enhancement effect on performance improvement of thermoelectric generator systems, Appl. Energy 263 (2020), 114688.
[65] C. Maduabuchi, Improving the performance of a solar thermoelectric generator using nano-enhanced variable area pins, Appl. Therm. Eng. 206 (2022), 118086.